Research Square

Preprints are preliminary reports that have not undergone peer review.
They should not be considered conclusive, used to inform clinical practice,
or referenced by the media as validated information.

Astragalus-Angelica sinensis-Derived Extracellular Vesicles Attenuate Knee Osteoarthritis with Periarticular Muscle Atrophy via PPARγ-Mediated Regulation of Skeletal Muscle Fatty Acid Metabolism

Dong Wang
Hangzhou Traditional Chinese Medicine Hospital Affiliated to Zhejiang Chinese Medical University
Yuhang Wang
the First Affiliated Hospital of Zhejiang Chinese Medical University (Zhejiang Provincial Hospital of Chinese Medicine)
Xuefeng Li
the First Affiliated Hospital of Zhejiang Chinese Medical University (Zhejiang Provincial Hospital of Chinese Medicine)
Junyu Lin
the First Affiliated Hospital of Zhejiang Chinese Medical University (Zhejiang Provincial Hospital of Chinese Medicine)
Tenghui Li
the First Affiliated Hospital of Zhejiang Chinese Medical University (Zhejiang Provincial Hospital of Chinese Medicine)
Wenzhe Chen
the First Affiliated Hospital of Zhejiang Chinese Medical University (Zhejiang Provincial Hospital of Chinese Medicine)
Kaiao Zou
the First Affiliated Hospital of Zhejiang Chinese Medical University (Zhejiang Provincial Hospital of Chinese Medicine)
Xu Wang
the First Affiliated Hospital of Zhejiang Chinese Medical University (Zhejiang Provincial Hospital of Chinese Medicine)
Haipeng Huang
the First Affiliated Hospital of Zhejiang Chinese Medical University (Zhejiang Provincial Hospital of Chinese Medicine)
Jingyuan Wen

the First Affiliated Hospital of Zhejiang Chinese Medical University (Zhejiang Provincial Hospital of Chinese Medicine)

Zhengsheng Bao

the First Affiliated Hospital of Zhejiang Chinese Medical University (Zhejiang Provincial Hospital of Chinese Medicine)

Jun Ying

the First Affiliated Hospital of Zhejiang Chinese Medical University (Zhejiang Provincial Hospital of Chinese Medicine)

Jiali Chen

the First Affiliated Hospital of Zhejiang Chinese Medical University (Zhejiang Provincial Hospital of Chinese Medicine)

Hongting Jin

hongtingjin@163.com

the First Affiliated Hospital of Zhejiang Chinese Medical University (Zhejiang Provincial Hospital of Chinese Medicine)

Research Article

Keywords: Knee osteoarthritis, Muscle atrophy, Astragalus membranaceus, Angelica sinensis, Extracellular vesicles, fatty acid metabolism, PPARγ

Posted Date: August 20th, 2026

DOI: https://doi.org/10.21203/rs.3.rs-10556770/v1

License: This work is licensed under a Creative Commons Attribution 4.0 International License. Read Full License

Additional Declarations: No competing interests reported.

Abstract

Knee osteoarthritis (KOA) is frequently accompanied by periarticular muscle atrophy. Targeting muscle atrophy holds promise for delaying KOA progression; however, therapeutic strategies that simultaneously protect both muscle and joint remain scarce. The traditional Chinese formula Danggui Buxue Decoction (DBD) shows potential in attenuating KOA-associated muscle atrophy, yet its clinical application is hindered by poor stability, low bioavailability, and insufficient tissue targeting. Plant-derived extracellular vesicles (EVs), as natural nanocarriers, can effectively overcome these limitations, and fresh herbs retain higher levels of bioactive constituents than their dried counterparts. In this study, we integrated traditional formula compatibility, fresh herb extraction, and EV isolation techniques to prepare nanovesicles from fresh Astragalus membranaceus and Angelica sinensis, and combined them at the 5:1 ratio of DBD to obtain Astragalus-Angelica sinensis-Derived Extracellular Vesicles (AA-EVs). AA-EVs were then characterized by TEM, zeta potential analysis, nanoparticle tracking analysis, and LC-MS. In an anterior cruciate ligament transection (ACLT)-induced mouse model of KOA with periarticular muscle atrophy, oral administration of AA-EVs dose-dependently ameliorated muscle atrophy, restored muscle mass and motor function, and delayed KOA progression, with overall therapeutic efficacy significantly superior to that of DBD decoction. In the TNF-α-stimulated C2C12 myotube atrophy model, AA-EVs inhibited myotube diameter reduction, restored the expression of myogenic regulatory factors MyoD and MyoG, suppressed the atrophy-related ubiquitin ligases Murf-1 and Atrogin-1, and reduced lipid droplet accumulation as well as MDA and free fatty acid levels. Integrated transcriptomic and metabolomic analyses identified PPARγ signaling and fatty acid metabolism as the core pathways of AA-EVs effect on KOA. Mechanistically, AA-EVs upregulated PPARγ and fatty acid oxidation-related gene expression; siRNA-mediated knockdown of PPARγ abolished the protective effects of AA-EVs on myotube morphology, lipid accumulation, and myogenesis-related gene expression. This study confirms that AA-EVs alleviate periarticular muscle atrophy and delay KOA progression through PPARγ-mediated fatty acid metabolism, providing a new strategy for the treatment of KOA and periarticular muscle atrophy.

1. Introduction

Knee osteoarthritis (KOA) is the most common musculoskeletal disease in clinical practice[1, 2]. Periarticular muscle atrophy is a common sign in KOA patients[3, 4]. This condition not only constitutes an independent prodromal factor for the development of KOA[5], but its severity is also strongly positively correlated with KOA grade and accelerates disease progression[6]. In recent years, the critical regulatory role of muscle tissue in the development and progression of KOA has been increasingly elucidated[7], and both domestic and international authoritative guidelines have listed muscle strengthening exercise as a first-line treatment for KOA[8]. Therefore, targeting periarticular muscle atrophy as a core intervention node and exploring novel therapeutic strategies that can simultaneously improve muscle function and delay KOA progression are of substantial clinical and scientific significance[9].

Traditional Chinese medicine has a long history in treating KOA[10]. For KOA accompanied by periarticular muscle atrophy, traditional Chinese medicine attributes its core pathogenesis to dual deficiency of qi and blood, which leads to malnourishment of tendons and vessels and consequent muscle wasting. Accordingly, the therapeutic principle is to replenish qi and nourish blood. The classic formula Danggui Buxue Decoction (DBD), composed of Astragalus membranaceus and Angelica sinensis at a ratio of 5:1, is a representative prescription for supplementing qi and generating blood[11]. Modern pharmacological studies have demonstrated that DBD possesses anti-inflammatory and antioxidant activities[12], regulates glycolipid metabolism[13] and energy metabolism[14], and exerts protective effects against orthopedic diseases. Phytochemical analyses have further revealed that DBD is rich in various bioactive constituents. Astragalus polysaccharides enhance muscle protein synthesis while concurrently suppressing ubiquitin-proteasome-mediated degradation, thus attenuating muscle atrophy and ameliorating muscle performance[15, 16]; Furthermore, they alleviate oxidative stress and cellular senescence in chondrocytes[17]. Astragaloside IV improves myocyte energy metabolism[18] and inhibits inflammatory responses[19]. Ferulic acid and ligustilide from Angelica sinensis exhibit significant anti-inflammatory activities[20, 21]; Angelica sinensis polysaccharides can also alleviate mitochondrial damage in chondrocytes and improve energy metabolism[22], thus conferring joint protection. Collectively, these lines of evidence support the potential of DBD in ameliorating KOA with concomitant periarticular muscle atrophy. However, traditional herbal decoctions suffer from limitations including poor stability, low extraction efficiency of active components, inadequate oral bioavailability, and insufficient tissue targeting[23, 24]. Therefore, on the basis of preserving the compatibility essence of the original formula, developing novel drug delivery systems to enhance targeted efficacy on local muscle tissue represents an important topic worthy of further investigation.

Extracellular vesicles (EVs), as nanoscale carriers capable of delivering lipids, proteins, nucleic acids, and various bioactive molecules, are emerging as promising natural tools in the fields of intercellular communication and disease therapy[25, 26]. In the exploration of treatments for KOA and periarticular muscle atrophy, preclinical models and early-phase clinical trials have preliminarily confirmed the safety and efficacy of EVs[27]. Compared with conventional drugs, EVs exhibit certain advantages in stability, bioavailability, therapeutic efficacy, and targeting capability[28]. For instance, watercress-derived EVs can alleviate osteoarthritis by restoring circadian rhythms[29], while Chinese leek-derived EVs ameliorate muscle atrophy by regulating mitochondrial biogenesis and autophagy via the AMPK pathway[30]. Fresh herbs, as a characteristic therapy in traditional Chinese medicine, retain higher levels of volatile substances, enzymes, and other active constituents, and thus often display stronger anti-inflammatory and pro-repair effects than dried herbs[31–33]. Specifically, fresh Astragalus membranaceus contains 20%–30% more astragaloside IV than the dried form, enabling more potent inhibition of synovial inflammation; fresh Angelica sinensis is rich in ferulic acid glycosides, with antioxidant capacity approximately 1.5-fold that of the dried product. These lines of evidence support our hypothesis that, compared with conventional decoctions prepared from dried herbs, EVs derived from fresh Astragalus membranaceus and Angelica sinensis may possess superior stability, bioavailability, and targeting

capability, thereby achieving better therapeutic efficacy against KOA-induced periarticular muscle atrophy.

Based on this, the present study integrated traditional formula compatibility, fresh herb extraction, and EV isolation techniques to obtain extracellular vesicles from fresh Astragalus membranaceus and Angelica sinensis, which were then mixed at the DBD ratio of 5:1 to yield Astragalus-Angelica sinensis vesicles (AA-EVs), thereby inheriting the "replenishing qi and nourishing blood" principle of DBD. Using a TNF-α-induced C2C12 myotube atrophy model in vitro and an ACLT mouse model in vivo, we systematically evaluated the effects of AA-EVs on periarticular muscle atrophy and KOA progression. The results demonstrated that oral administration of AA-EVs significantly suppressed periarticular muscle atrophy in ACLT mice, delayed KOA progression, and exhibited superior stability, bioavailability, targeting capability, and therapeutic efficacy compared with traditional DBD decoction; concurrently, AA-EVs attenuated TNF-α-induced C2C12 myotube atrophy. Mechanistically, AA-EVs regulated skeletal muscle fatty acid metabolism through PPARγ signaling, thereby ameliorating periarticular muscle atrophy and delaying KOA progression in ACLT mice. Integrating in vitro and in vivo experiments with multi-omics analyses, this study systematically elucidated the mechanism by which AA-EVs alleviate KOA through targeting muscle atrophy, suggesting that AA-EVs may represent a promising new agent for the prevention and treatment of KOA accompanied by periarticular muscle atrophy.

2. Materials and methods

- **Preparation of DBD extract**
- The herbs for DBD were provided by Zhejiang Provincial Hospital of Traditional Chinese Medicine. To prepare DBD extract, 60 g of Astragalus membranaceus and 12 g of Angelica sinensis were first soaked in purified water. After half an hour, they were removed and 1.2 L of purified water was added. The mixture was heated and boiled for 1 h, then filtered through a strainer and the filtrate was collected. Another 1.2 L of purified water was added to the residue, and the decoction was continued for 1 h. After filtering through a strainer, the filtrate was collected. The first filtrate was mixed with the second filtrate and concentrated to 200 mL to obtain a herbal liquid with a crude drug content of 0.36 g/mL.

Analysis of physical and biochemical stability of AA-EVs

Fresh Astragalus membranaceus and Angelica sinensis sourced from Min County, Gansu Province, China, were selected as raw materials for the preparation of Astragalus-Angelica sinensis vesicles. The fresh herbs were washed three to four times with deionized water, air-dried, and thoroughly homogenized using a juicer. The resulting juice was initially filtered through gauze and then subjected to differential centrifugation at 4°C: 500 × g for 10 min, 2,000 × g for 20 min, 5,000 × g for 30 min, and 10,000 × g for 60 min. After each step, the supernatant was retained and the pellet discarded. The final supernatant was ultracentrifuged at 120,000 × g for 2 h. The resulting pellet was resuspended in phosphate-buffered saline (PBS) and passed through a 0.22 μm filter, yielding Astragalus-derived vesicles (As-EVs) and

Angelica sinensis-derived vesicles (An-EVs), respectively (workflow illustrated in Fig. 3A). The isolated As-EVs and An-EVs were either used immediately or stored at − 80°C. Vesicle morphology was examined by transmission electron microscopy (TEM, 200 kV, FEI Tecnai G2 F20). Hydrodynamic size and zeta potential were measured using a Malvern Zetasizer Nano ZSE (Malvern Instruments, UK), and particle concentration was determined by nanoparticle tracking analysis (NTA, Nanosight Pro, UK). Protein profiles were assessed by Coomassie Brilliant Blue staining (Beyotime, Shanghai, China). Additionally, liquid chromatography-mass spectrometry (LC/MS, Milford, MA, USA) combined with proteomic analysis was employed to systematically identify the bioactive components and protein composition of the EVs.

Cellular uptake assay

To trace the cellular internalization of As-EVs and An-EVs, the vesicles were labeled with the lipophilic fluorescent dyes CM-Dio (yellow) and CM-Did (red), respectively. Both dyes were separately dissolved in dimethyl sulfoxide (DMSO) to prepare 1 mM stock solutions and then diluted 100-fold with PBS to obtain 10 μM working solutions. The vesicle suspensions were incubated with the working solutions at 37°C for 5 min and then transferred to 4°C for an additional 15 min to complete the fluorescent labeling. After 24 h of uptake, C2C12 cells exposed to the labeled vesicles were stained with 488-phalloidin (green; Yeasen) for the cytoskeleton and DAPI (blue; Beyotime) for nuclei. The combination of these probes made it possible to directly visualize and track the endocytic processes of As-EVs and An-EVs by confocal laser scanning microscopy.

Uptake of As-EVs by C2C12 cells

To assess the cellular uptake efficiency of AA-EVs, the vesicles were labeled by incubation with 10 μM lipophilic fluorescent dye Dio in the dark for 30 min, after which free dye was removed by differential ultracentrifugation. The Dio-labeled AA-EVs were then added to C2C12 cells in serum-free medium at a final concentration of 10×10^8 particles/mL and co-incubated for 3, 6, 12, and 24 h. The proportion of Dio-positive cells was quantified by flow cytometry to evaluate the extent of internalization.

- **Cell culture and treatments**

C2C12 myoblasts were propagated in growth medium consisting of DMEM (Gibco, USA) containing 10% fetal bovine serum, 100 IU/mL penicillin, and 0.1 mg/mL streptomycin, and maintained at 37°C in a 5% CO_2 atmosphere. Myogenic differentiation was induced by replacing the growth medium with differentiation medium (DMEM supplemented with 2% horse serum and the identical antibiotic cocktail) and culturing the cells for an additional 5 days.

- **Cell viability**

Cell viability was determined with the CCK-8 kit (Beyotime, China). C2C12 cells were plated in 96-well plates at 5×10^3 cells/well in 100 μL of complete medium. After 24 h of attachment and growth, the cells were exposed to AA-EVs at 0, 5, 10, 20, 50, 100, 200, or 500×10^7 particles/mL, with or without 100 μM TNF-α (a dose chosen based on previous reports), and incubation continued for another 24 h.

Subsequently, 10 μL of CCK-8 reagent was introduced per well and kept at 37°C for 30 min. Absorbance at 450 nm was recorded on a Bio-Rad microplate reader. Six independent biological replicates were set up for each condition.

Measurement of C2C12 myotube diameter

After differentiation, C2C12 myotubes were stained with Giemsa and their morphological characteristics were observed under a light microscope. C2C12 cells were seeded into 6-well plates and induced to differentiate into myotubes. Four experimental groups were established: control group (CON), TNF-α group (100 μM TNF-α), and two AA-EVs intervention groups (100 μM TNF-α combined with 5×10^8 or 10×10^8 particles/mL AA-EVs), with five replicates per group. After five days of differentiation, the cells were treated according to the above grouping for 24 h. Approximately 50 myotubes were measured per well, yielding approximately 250 myotubes per group, and each myotube was measured three times to obtain an average value.

RNA extraction and quantitative real-time polymerase chain reaction (qRT-PCR)

- Total RNA was isolated from C2C12 cells with TRIzol reagent (Invitrogen, USA) following the manufacturer's protocol. RNA quantity and purity were determined by measuring the absorbance at 260 and 280 nm. First-strand cDNA was generated using the PrimeScript RT reagent kit (Biosharp, Guangzhou, China). Gene expression was subsequently analyzed by quantitative real-time PCR employing the SYBR Premix Ex Taq kit (Biosharp, Guangzhou, China). The thermal profile comprised an initial denaturation step at 95°C for 1 min, followed by 40 cycles of 90°C for 30 s and 60°C for 30 s. Melt curve analysis was performed by heating to 95°C for 15 s and 60°C for 1 min. β-Actin was used as the endogenous control, and relative mRNA levels were calculated by the $2^{-}\Delta\Delta Ct$ method. All assays were conducted in three independent experiments, and the primers are listed in Table S4.
- **Western blotting (WB)**
- C2C12 myotubes were rinsed three times with PBS and then incubated with ice-cold RIPA lysis buffer on ice for 30 min. Cells were scraped off the plate, and the lysate was centrifuged to collect the protein-containing supernatant. The samples were mixed with 5× loading buffer (Beyotime, China) and heated at 100°C for 10 min to ensure complete denaturation. Equal amounts of protein were resolved by SDS-PAGE on 7.5%–15% gradient gels, chosen according to the molecular weights of the target proteins, and subsequently electroblotted onto PVDF membranes. After blocking in blocking solution for 1 h at room temperature, the membranes were probed with the following primary antibodies at 4°C overnight: GAPDH (1:5000), β-actin (1:10000), Murf-1 (1:1000), MyoG (1:1000), and PPARγ (1:1000). Following TBST washes, the membranes were incubated with HRP-conjugated secondary antibodies (1:5000) for 1 h at room temperature. Immunoreactive bands were detected by chemiluminescence using a Bio-Rad ChemiDoc XRS system after immersion in developing solution. β-Actin served as the internal control, and densitometric quantification was performed with ImageJ software.
- **Animal**

- All animal experimental protocols were reviewed and approved by the Animal Ethics Committee of Zhejiang Chinese Medical University and performed in strict accordance with institutional guidelines. Six- to eight-week-old C57BL/6 mice were utilized throughout the study.
- **Murine models of sarcopenia and their treatment**
- An anterior cruciate ligament transection (ACLT) procedure was employed to establish a mouse model of knee osteoarthritis accompanied by muscle atrophy. Following intraperitoneal anesthesia with Zoletil 50 (50 mg/kg), a longitudinal skin incision was made over the right knee joint, and the anterior cruciate ligament was resected under a surgical microscope using an ophthalmic scalpel. Twenty-four hours after surgery, the mice were randomly assigned to the following groups, and oral gavage treatment was initiated on postoperative day seven. To evaluate the interventional effects of DBD, the groups included a sham group (arthrotomy without ligament transection, gavaged with PBS), an ACLT group (ACLT + PBS gavage), a low-dose DBD group (DBD-L, 5.4g/kg/d), and a high-dose DBD group (DBD-H, 10.8g/kg/d). To assess the therapeutic efficacy of AA-EVs, additional groups were established: sham group, ACLT group, low-dose AA-EVs group (5×10^8 particles/mL), and high-dose AA-EVs group (10×10^8 particles/mL). Each group consisted of six mice, and oral gavage was performed once daily for four consecutive weeks. Body weight changes were monitored dynamically. Four weeks after surgery, behavioral tests were conducted, after which the mice were sacrificed. The right knee joint, tibialis anterior, quadriceps, and gastrocnemius muscles were harvested for subsequent analyses.

Pain-Related Behavioral Assessment

Mechanical nociception was assessed with von Frey filaments (0.008–300 g; Stoelting Co., USA). Starting from a 0.16-g filament, the probes were applied perpendicularly to the central plantar surface of the right hind paw, and the 50% withdrawal threshold was determined using the up-down paradigm.

Thermal nociception was evaluated on a YLS-6B intelligent hot-plate device (Mouse Specifics, USA) with the surface temperature maintained at 50.0 ± 0.5°C. The time until the mouse licked its right hind paw or jumped was recorded. Five measurements were taken per animal at 5-min intervals, and the mean was adopted as the heat pain threshold.

Grip Strength Test

A grip strength meter was used to evaluate the forelimb grip force. Prior to each test, the device was zeroed. Mice were then placed horizontally on the grip platform, allowing their forelimbs to firmly grasp the bar. The tail was pulled backward with uniform force until the forelimbs released, and the maximum grip force value was recorded. Each mouse was tested three consecutive times, and the average was taken as the representative grip strength for that individual.

Gait Analysis

Gait analysis was performed using the DigiGait system (Mouse Specifics, USA). According to previously described methods, mice were placed on a motorized treadmill and forced to run at a constant speed of 18 cm/s, while gait video sequences were captured at 200 frames/s for 6–10 seconds. The analyzed parameters included swing time (s), stance time (s), stride length (cm), and peak stance-phase footprint area (cm^2).

Open Field Test

The open field test was conducted in a flat, open arena with clearly defined boundaries. Prior to formal recording, mice underwent multiple habituation sessions (5–10 min each) to familiarize themselves with the environment, thereby reducing novelty-induced stress and experimental variability. During the 5–10 min test period, spontaneous locomotor activity and total distance traveled were automatically recorded using an infrared tracking device.

The cross-sectional area of muscle fibers in mice

The tibialis anterior (TA), quadriceps (Quad), and gastrocnemius (Gast) muscles were harvested from mice in each group and processed according to standard histological protocols. Tissues were fixed, embedded in paraffin, and cut into transverse sections. These sections were then subjected to hematoxylin–eosin (H&E) and Masson's trichrome staining. For each animal, 100 myofibers were randomly selected from representative cross-sections, and the cross-sectional area (CSA) of each fiber was quantified with ImageJ software.

Micro-CT scanning

Right knee joints were fixed in 4% paraformaldehyde for 72 h and then scanned with a high-resolution micro-CT system (SkyScan 1275, Bruker, Belgium). The region of interest (ROI) was delineated as the zone between the proximal tibial growth plate and the tibial plateau. Three-dimensional reconstruction was carried out with NRecon software, and subchondral bone histomorphometry was subsequently performed using DataView. CTVox and Mimics Research were applied for model visualization and structural evaluation. Finally, the bone volume fraction (BV/TV) was computed to quantify alterations in the trabecular microarchitecture of the joint.

Histological Analysis

Right knee joint samples were fully fixed in 4% paraformaldehyde, decalcified in 14% EDTA for 14 days, and subsequently dehydrated through graded alcohols using a Tissue-Tek VIP 5 Jr automated processor (Japan) before being embedded in paraffin. Serial sagittal sections (4 μm) were cut, deparaffinized with xylene, rehydrated in a descending ethanol series, differentiated in acidified alcohol, and finally stained with ABH/OG for cartilage visualization. All stained slides were digitized with a whole-slide imaging system (3DHISTECH PANNORAMIC MIDI II, Hungary). Cartilage lesions were assessed semiquantitatively according to the OARSI scoring system by three independent evaluators experienced in orthopedic pathology, who were blinded to the experimental groups.

IHC and IF

Paraffin sections were heated at 60°C for 4 h, deparaffinized in xylene, rehydrated through a graded ethanol series, and subjected to antigen retrieval in citrate buffer (pH 6.0) at 60°C for 4 h. After rinsing with PBS, the sections were permeabilized with Triton X-100 for 10 min and blocked with 5% goat serum (1:20) at room temperature for 20 min. The sections were then incubated overnight at 4°C with primary antibodies against COL2, MMP-13, MyoG, Murf-1, and PPARγ, all diluted at 1:200. On the following day, the slides were divided for either immunohistochemistry (IHC) or immunofluorescence (IF) detection.

For IHC, HRP-conjugated secondary antibodies were applied and incubated for 30 min at room temperature. After development with DAB chromogen, the sections were counterstained with hematoxylin for 20 s, dehydrated, coverslipped, and digitized using a whole-slide scanning system (3DHISTECH PANNORAMIC MIDI II, Hungary).

For IF, the sections were incubated with Alexa Fluor® 488-conjugated anti-rabbit IgG (1:1000) at 37°C for 40 min in the dark. Following PBS washes, nuclei were labeled with DAPI (1:1000) for 10 min. Fluorescence images were captured with a Zeiss LSM880 laser scanning confocal microscope and quantitatively analyzed using ImageJ software.

Oil Red O Staining

Lipid droplets and lipid deposition in mouse muscle tissues and C2C12 myoblasts were stained using a Modified Oil Red O Staining Kit (C0158S, Beyotime Biotechnology, Shanghai, China) strictly in accordance with the manufacturer’s instructions.

Nile Red Staining

Lipid droplets in C2C12 myoblasts were stained using a Nile Red Staining Kit (C2051S, Beyotime Biotechnology, Shanghai, China) strictly in accordance with the manufacturer's instructions.

Malondialdehyde (MDA) Assay

The malondialdehyde (MDA) content in C2C12 myoblasts was determined using a Lipid Peroxidation MDA Assay Kit (S0131S, Beyotime Biotechnology, Shanghai, China) strictly according to the manufacturer's instructions, with colorimetric measurement performed at a wavelength of 532 nm.

Amplex Red Free Fatty Acid Assay

The free fatty acid content in C2C12 myoblasts was determined using an Amplex Red Free Fatty Acid Assay Kit (S0215S, Beyotime Biotechnology, Shanghai, China) strictly according to the manufacturer's instructions, with colorimetric measurement performed at a wavelength of 570 nm.

Statistical analysis

All values are expressed as the mean ± standard deviation (SD). Statistical analysis and graphing were performed using GraphPad Prism 10 (version 10.1.2). After verification of normal distribution and equal variances, group differences were assessed as follows: two-group comparisons were made with an independent-samples t-test, and comparisons involving three or more groups were carried out by one-way analysis of variance (ANOVA) followed by Tukey's post hoc test for pairwise evaluations. A P value < 0.05 was considered statistically significant. Asterisks in the figures denote significance levels as follows: ns, no significant; *P < 0.05; **P < 0.01; ***P < 0.001.

3. Results

Periarticular Muscle Atrophy During the Progression of KOA

Based on clinical observations, this study performed a systematic review of knee X-ray and magnetic resonance imaging (MRI) data from patients with different Kellgren-Lawrence (K-L) grades. Imaging evidence clearly showed that as the K–L grade increased, the degree of periarticular muscle atrophy progressively worsened (Fig. 1A), indicating that muscle atrophy is closely related to the clinical severity of KOA.

To validate the above clinical observations and explore potential interventional strategies, we further established a mouse model of KOA with periarticular muscle atrophy using anterior cruciate ligament transection (ACLT) and dynamically evaluated the temporal association between joint degeneration and muscle atrophy[9, 34]. Three-dimensional micro-CT reconstructions of the knee joints showed that as KOA progressed, subchondral bone loss gradually increased in ACLT mice (Fig. 1B). Histopathological analysis further confirmed that the severity of KOA joint pathology increased over time after ACLT. In parallel, the cross-sectional areas (CSA) of muscle fibers in the quadriceps, gastrocnemius, and tibialis anterior muscles progressively declined (Fig. 1C). Linear correlation analysis demonstrated that BV/TV was positively correlated with muscle fiber CSA, while the OARSI score was negatively correlated with CSA (Fig. 1D). These results indicate that the more severe the joint structural damage, the greater the degree of muscle atrophy, and a significant linear correlation exists between the two, providing direct experimental evidence for subsequent therapeutic strategies targeting muscle atrophy to intervene in KOA progression.

DBD Attenuates ACLT-Induced Skeletal Muscle Atrophy and Promote Muscle Mass, Regeneration, and Function

Given the above findings confirming the close association between KOA progression and muscle atrophy, we subsequently explored the interventional potential of the classic formula DBD, which has the effects of replenishing qi and nourishing blood, on periarticular muscle atrophy. C57BL/6J mice underwent ACLT modeling, and from the 7th day after surgery, DBD was administered daily by oral gavage, with body weight continuously monitored during the experiment. After 28 consecutive days of administration, the therapeutic effect of DBD was evaluated by multimodal assessment including muscle mass quantification, functional tests, and kinematic analysis (Fig. 2A). Before the experiment, there were

no statistical differences in body weight among the groups; compared with the sham group, the body weight of the ACLT model group decreased significantly. Compared with the ACLT group, the body weight of mice in the high-dose DBD (DBD-H) group recovered to some extent, but was still lower than that of the sham group (Fig. 2B). Behavioral analysis showed that DBD dose-dependently increased mouse grip strength (Fig. S1A), prolonged thermal pain latency (Fig. S1B), and extended swimming time (Fig. S1C). At the same time, DBD effectively improved gait parameters, including prolonged stance time, increased stride length, and enlarged footprint area (Fig. S1D, E). The open field test showed that, compared with the ACLT group, mice in the DBD-treated group had more active movement trajectories and significantly longer total distance traveled (Fig. S1F, G). All the above behavioral indices showed dose-dependent improvement, among which the DBD-H group showed the most significant effect, but none of the indices returned to the sham group level. These results indicated that DBD could partially alleviate ACLT-induced decline in muscle strength and motor dysfunction.

Subsequently, the quadriceps, gastrocnemius, and tibialis anterior muscles as well as the internal organs of mice in each group were collected for comprehensive evaluation. The representative comparison of muscle sizes among groups is shown in the figure (Fig. 2C), and pathological staining confirmed that DBD had good biosafety (Fig. S2). Muscle mass measurements revealed a significant decrease in the ACLT group compared with the sham group, which was reversed by DBD treatment in a dose-dependent manner, suggesting that DBD preserved muscle weight (Fig. 2D). Histological analysis of the quadriceps, gastrocnemius, and tibialis anterior muscles demonstrated that DBD markedly alleviated the ACLT-induced reduction in fiber cross-sectional area (CSA) (Fig. 2E, G). To evaluate muscle regenerative capacity, the quadriceps was stained for MyoG and MuRF-1 by immunofluorescence. MyoG is a key transcription factor in the myogenic regulatory factor family, serving as an early marker of myogenic differentiation that drives myoblast fusion and myotube formation[35]; MuRF-1 belongs to the muscle-specific E3 ubiquitin ligase family, is upregulated during muscle atrophy, mediates ubiquitination-dependent degradation of myofibrillar proteins, and drives muscle protein breakdown, making it a commonly used molecular marker of skeletal muscle atrophy[36]. The immunofluorescence results showed the expected trend of changes (Fig. 3F, H): compared with the sham group, MyoG expression in the ACLT group was significantly inhibited, while MuRF-1 expression was markedly increased; after DBD intervention, the above changes were reversed in a dose-dependent manner, although they did not recover to the sham group level. These results indicated that DBD could inhibit muscle protein degradation and promote anabolic metabolism, thereby partially improving ACLT-induced periarticular muscle atrophy.

Isolation, characterization and compositional analysis of AA-EVs

The above results indicated that DBD had a certain protective effect on ACLT-induced skeletal muscle atrophy, but all indices did not return to the sham group level, indicating that the therapeutic efficacy of traditional decoction was still limited. To overcome the above deficiencies and retain the compatibility essence of the original formula, we further directly prepared nanovesicles from fresh Astragalus

membranaceus and Angelica sinensis, mixed them at a 5:1 ratio to obtain AA-EVs, and performed systematic isolation, characterization, and compositional analysis of them.

The fresh Astragalus membranaceus and Angelica sinensis were respectively juiced, and Astragalus membranaceus extracellular vesicles (As-EVs) and Angelica sinensis extracellular vesicles (An-EVs) were obtained by differential centrifugation, followed by purification and comprehensive characterization (Fig. 3A). Transmission electron microscopy showed that both As-EVs and An-EVs were elliptical vesicles with an average diameter of approximately 180 nm (Fig. 3C). Zeta potential analysis showed that the surface charge of As-EVs was − 12 mV, and that of An-EVs was − 4 mV (Fig. 3D). Western blot analysis showed that As-EVs and An-EVs were positive for HSP70 signal (Fig. S3). Nanoparticle tracking analysis indicated that the particle concentration of As-EVs was 2.29×10^{8} particles/ml, and that of An-EVs was 7.86×10^{8} particles/ml. Tyndall effect detection showed that the suspensions of As-EVs, An-EVs, and Astragalus-Angelica sinensis-Derived Extracellular Vesicles (AA-EVs) were all homogeneous and stable. To further evaluate the stability of AA-EVs under physiological conditions, they were placed in simulated gastric fluid (SGF) and simulated intestinal fluid (SIF) buffers, incubated at 37°C, and then the Tyndall effect was detected. The results showed that under both gastric fluid and intestinal fluid conditions, the light scattering intensity remained uniform and stable, indicating that the structural integrity of AA-EVs was maintained in a physiological environment (Fig. 3E). Coomassie brilliant blue staining results showed that As-EVs, An-EVs, and AA-EVs all presented complete protein profiles, confirming that their protein composition remained intact (Fig. 3B).

To evaluate the muscle cell uptake efficiency of AA-EVs, flow cytometry analysis showed that the proportion of fluorescent-positive C2C12 cells gradually increased with prolonged incubation time; after 24 h of incubation with AA-EVs, the proportion of positive cells reached 89.9% (Fig. 3F). Confocal microscopy imaging further confirmed that DiO-labeled AA-EVs could be internalized by C2C12 cells after 24 h of co-incubation (Fig. 3G).

To evaluate the in vivo retention characteristics and targeting ability of AA-EVs, free ICG and ICG-labeled AA-EVs were separately administered to mice by oral gavage in two groups, and major organs were collected at 6, 12, 24, and 48 h after administration for ex vivo fluorescence imaging. The results showed that compared with free ICG, the AA-EVs group showed no significant difference in fluorescence signal in the liver region, suggesting no obvious interference with liver metabolism; whereas in muscle and bone tissues, AA-EVs exhibited stronger targeting and significantly prolonged retention time (Fig. 3F).

Under optimized conditions, total ion chromatograms (TIC) were acquired by LC-MS in positive ion (POS) and negative ion (NEG) modes, respectively. Component identification showed that As-EVs contained a total of 15 bioactive components, with the following detected in negative ion mode: L-Arginine; Isococculidine; 4-Hydroxy-3-methoxycinnamic acid; 2-Hydroxy-4-allylphenyl 6-O-α-L-rhamnopyranosyl-β-D-glucopyranoside; Azelaic acid; Senkyunolide D; Acetylastragaloside. The following were detected in positive ion mode: Glycogen; Adenine; Guanosine; Riboflavin; 7,2'-Dihydroxy-3',4',6'-trimethoxyisoflavan; Phellatin; Carvacryl acetate; Suchilactone (Fig. S4, Table S1). An-EVs contained a total of 14 bioactive

components, with the following detected in negative ion mode: 4-Hydroxy-3-methoxycinnamic acid; Azelaic acid; Astragaloside VII; Senkyunolide D; Astragaloside III; Acetylastragaloside; Isoastragaloside II. The following were detected in positive ion mode: Glycogen; Adenine; Guanosine; Rosifoliol; Phellatin; Prostaglandin E2; Suchilactone (Fig. S5, Table S2). AA-EVs were identified to contain 20 bioactive components, completely covering all the identified components in As-EVs and An-EVs, indicating that AA-EVs retained the main bioactive components of both (Fig. 3H, Table S3).

In summary, the above results confirmed that AA-EVs with well-defined physicochemical properties had been successfully obtained. LC-MS analysis further showed that AA-EVs were rich in a variety of bioactive components that may be involved in host metabolic regulation, laying a material basis for their subsequent efficacy evaluation in the KOA accompanied by periarticular muscle atrophy model.

AA-EVs Restore Myogenic Differentiation in C2C12 Cells and Ameliorate Periarticular Muscle Atrophy in ACLT Mice

To explore the therapeutic effect of AA-EVs on muscle atrophy, C2C12 myoblasts were induced to differentiate into myotubes, then treated with 100 μM TNF-α for 24 h to establish a myotube atrophy model[37, 38], and subsequently intervened with different concentrations of AA-EVs (0–500 × 10^7 particles/mL) for 24 h. CCK−8 assay showed that AA-EVs pretreatment in the range of 0–100 × 10^7 particles/mL itself had no cytotoxicity (Fig. S6), but could dose-dependently alleviate the decrease in cell viability caused by TNF-α (Fig. 3D). Dose-response relationship analysis determined 50 × 10^7 particles/mL as the optimal protective concentration, and accordingly two dose gradients were selected for subsequent mechanism research: low-dose group (AA-EVs-L, 10×10^7 particles/mL) and high-dose group (AA-EVs-H, 50×10^7 particles/mL). Giemsa staining experiment showed that compared with TNF-α treatment alone, AA-EVs protected myotube diameter in a dose-dependent manner (Fig. 4A, C). Myosin heavy chain (MyHC) immunofluorescence staining results further supported this finding (Fig. 4B, D). The ubiquitin-proteasome system is the main pathway for muscle protein degradation. Atrogin−1 and MuRF1 both belong to the E3 ubiquitin ligase family and play key regulatory roles in muscle atrophy[39]. Myogenic differentiation 1 (MyoD) and MyoG are both core members of the myogenic regulatory factor family and are early markers of myogenic differentiation initiation; MyoD also participates in regulating myoblast proliferation[40]. qPCR analysis of the above four key genes showed the expected change trend: TNF-α significantly inhibited MyoD/MyoG expression and simultaneously upregulated MuRF1/Atrogin−1; AA-EVs treatment dose-dependently reversed these changes (Fig. 4E). Western blot experiments further verified the changes of MuRF−1 and MyoG at the protein level, and the results were consistent with the mRNA trend (Fig. 4F, G). The above in vitro results indicated that AA-EVs could effectively counteract TNF-α-induced C2C12 myotube atrophy and restore their myogenic differentiation ability.

Based on the above in vitro results, we further evaluated the in vivo efficacy of AA-EVs on muscle atrophy in the ACLT mouse model. The intervention protocol was the same as DBD. After ACLT modeling, AA-EVs or DBD was administered daily by oral gavage from the 7th day for 28 consecutive days. Subsequently,

multimodal assessment including muscle mass quantification, functional tests and kinematic analysis was performed to evaluate the treatment outcome. Body weight was monitored throughout the intervention period: there was no significant difference in baseline body weight among the groups; the ACLT group showed significant body weight decrease after surgery, while AA-EVs dose-dependently recovered body weight, and the recovery effect was better than that of DBD. Among them, the body weight recovery degree of the low-dose AA-EVs group (AA-EVs-L) was comparable to that of the high-dose DBD group (DBD-H), and the high-dose AA-EVs group (AA-EVs-H) had recovered body weight to the sham group level after 28 days of administration (Fig. S7A). Thermal pain latency (Fig. S7B), grip strength (Fig. S7C) and swimming time (Fig. S7D) tests all showed dose-dependent improvement in muscle function; the effect of the AA-EVs-L group was comparable to that of DBD-H, and each index in the AA-EVs-H group all recovered to the sham group level. At the same time, AA-EVs effectively improved gait parameters, including shortening and prolonging stance time, increasing stride length and footprint area (Fig. S7E), among which the effect of the AA-EVs-H group was better than that of the DBD group, and could recover to the sham group level. In the open field test, compared with the DBD-H group, mice in the AA-EVs-H group had more active movement trajectories and significantly longer total distance traveled (Fig. S7F). The above results indicated that compared with the traditional formula DBD, AA-EVs could more effectively inhibit ACLT-induced muscle strength decline and motor dysfunction.

After the behavioral tests, the mice were sacrificed and sampled. The quadriceps, gastrocnemius and tibialis anterior muscles of mice in each group were collected for comprehensive evaluation; representative muscle appearance is shown in Fig. 4H. Then the muscles were weighed: the muscle mass of the AA-EVs-L group rose to a level comparable to that of the DBD-H group, while the AA-EVs-H group basically recovered to the normal level (Fig. 4J). Histological analysis showed that AA-EVs treatment significantly reversed the ACLT-induced reduction in muscle fiber cross-sectional area (CSA) (Fig. 4I, K, Fig. S9); compared with DBD-H, the CSA improvement in the AA-EVs-H group was more significant and had no statistical difference from the sham group. Subsequently, immunofluorescence staining of MyoG and Murf–1 further confirmed that the ability of AA-EVs to promote muscle regeneration was better than that of DBD (Fig. 4L, Fig. S10 A, B). In addition, pathological staining confirmed that AA-EVs had good biosafety (Fig. S8). In summary, AA-EVs counteracted ACLT-induced muscle atrophy in a dose-dependent manner; their overall improvement in muscle mass, muscle fiber size, and myogenic/catabolic markers was superior to that of the traditional formula DBD, and high-dose AA-EVs could restore each index basically to the normal level.

Metabolomic Profiling Reveals the PPAR Pathway and Fatty Acid Metabolism as Potential Mechanisms Underlying the Effects of AA-EVs

To further elucidate the molecular mechanisms underlying the protective effects of AA-EVs against muscle atrophy, we performed transcriptomic sequencing on quadriceps femoris muscles from mice in the Sham, ACLT, and AA-EVs-treated groups. Volcano plots visualized the differentially expressed genes (DEGs) between groups. Specifically, 622 DEGs were identified between the ACLT and Sham groups, with 578 upregulated and 44 downregulated. In the AA-EVs vs. ACLT comparison, 655 DEGs were detected,

among which 240 were upregulated and 415 were downregulated (Fig. 5A). A Venn diagram illustrated the overlapping DEGs between the two comparisons (Fig. 5B). Hierarchical clustering heatmaps demonstrated that transcriptomic profiles were clearly segregated by treatment conditions, with no apparent batch effects observed (Fig. S11).

- To characterize the functional attributes of the differentially expressed genes (DEGs), Gene Ontology (GO) enrichment analysis revealed that the biological processes modulated by AA-EVs treatment were predominantly enriched in lipid metabolism-related terms, including lipid metabolic process, lipid droplet, brown fat cell differentiation, fatty acid metabolic process, white fat cell differentiation, fat cell differentiation, negative regulation of lipid catabolic process, fatty acid biosynthetic process, and triglyceride biosynthetic process (Fig. 5E). Furthermore, KEGG pathway enrichment analysis indicated that the DEGs in the AA-EVs vs. ACLT comparison were significantly enriched in the regulation of lipolysis in adipocytes and the PPAR signaling pathway (Fig. 5F), both of which serve as central regulatory hubs for lipid metabolism and fatty acid oxidation[41]. To further evaluate the degree of pathway perturbation, we performed Gene Set Enrichment Analysis (GSEA). The results showed that the lipoic acid metabolism pathway was suppressed in the ACLT group ($P = 0.011$), lipoic acid metabolism is essential for cell growth, mitochondrial function, and the coordinated utilization of multiple fuel substrates; its inhibition may suppress fatty acid oxidation and consequently promote lipid accumulation[42]. Notably, AA-EVs treatment significantly upregulated this pathway ($P < 0.001$) and concurrently activated the PPAR signaling pathway ($P < 0.001$) (Fig. 5G).
- Subsequently, metabolomic sequencing was performed on quadriceps muscles from the same three groups. Metabolomic profiling revealed that ACLT modeling and AA-EVs treatment significantly altered the muscle metabolite landscape. Volcano plots illustrated the differentially abundant metabolites between groups: 351 metabolites were identified between the ACLT and Sham groups (257 upregulated, 94 downregulated), while 227 differential metabolites were detected between the AA-EVs and ACLT groups (93 upregulated, 134 downregulated) (Fig. S12A). Among the 94 metabolites downregulated in the ACLT group relative to the Sham group, AA-EVs treatment selectively restored 7 metabolites back to Sham levels, indicating a reversal of ACLT-induced metabolic suppression. Conversely, among the 257 metabolites upregulated in the ACLT group, AA-EVs significantly downregulated 14 metabolites, shifting them toward Sham levels and counteracting ACLT-induced metabolite elevation (Fig. S12B). KEGG pathway enrichment analysis of differential metabolites (top 20 pathways ranked by ascending P-value, Fig. S12C) revealed that both comparisons (ACLT vs. Sham and AA-EVs vs. ACLT) converged on pathways intimately associated with fatty acid metabolism, including central carbon metabolism in cancer, pantothenate and CoA biosynthesis[43–45], and ABC transporters[46, 47]. Hierarchical clustering analysis of 61 pathway-associated metabolites (Fig. S12D) demonstrated a clear remodeling of the muscle fatty acid metabolic profile mediated by AA-EVs. Specifically, compared with the ACLT group, AA-EVs treatment resulted in the downregulation of multiple lipid metabolites in muscle, including 13-keto myristic acid, trans-gondoic acid, 3S-hydroxypalmitic acid, 5S,6S-epoxy-7-undecenoic acid, 2,15-

dihydroxy-pentadecylic acid, petroselaidic acid, and 9,10,11-trihydroxy-12Z-octadecenoic acid. Collectively, these transcriptomic and metabolomic reprogramming effects suggest that AA-EVs may counteract muscle atrophy by mediating fatty acid metabolic homeostasis, with the PPAR signaling pathway potentially serving as a key regulatory axis.

AA-EVs Regulate Fatty Acid Metabolism via PPARγ Signaling to Ameliorate Muscle Atrophy

Integrated transcriptomic and metabolomic analyses suggested that the PPAR signaling pathway and fatty acid metabolism may be the potential mechanisms by which AA-EVs counteract muscle atrophy. To verify this finding, we systematically examined lipid deposition, fatty acid metabolism markers, and the expression changes of PPAR family members (PPARα, PPARβ, PPARγ) in in vivo and in vitro models.

In the in vivo aspect, Oil Red O staining was first performed on the quadriceps muscle cross-sections of ACLT mice. The results showed that a large amount of lipid droplets accumulated within the muscle fibers of the ACLT group, while AA-EVs intervention could dose-dependently reduce lipid deposition (Fig. 6A, B). Subsequently, qPCR verification of fatty acid metabolism markers and the PPAR family was performed using transcriptome sequencing samples. The results showed that ACLT modeling and AA-EVs intervention had no significant effect on the expression of genes related to muscle fatty acid synthesis and uptake, as well as PPARα and PPARβ (Fig. S13); however, after ACLT modeling, the expression of fatty acid oxidation-related genes and PPARγ was significantly downregulated, and AA-EVs intervention could effectively restore the expression levels of the above genes (Fig. 6C, D). The traditional view holds that PPARα more directly controls fatty acid oxidation[48], but many studies have confirmed that activation of PPARγ can promote fatty acid oxidation and reduce lipid deposition[49]. Moreover, studies have shown that the traditional formula Sanmiao pill can improve macrophage fatty acid metabolism disorder by activating PPARγ[50], and PPARγ activity is also necessary for skeletal muscle regeneration[51]. The above results together with existing studies suggest that AA-EVs may regulate skeletal muscle fatty acid metabolism via PPARγ. Immunofluorescence staining further confirmed that the fluorescence intensity of PPARγ in the muscle fibers of the ACLT group was significantly weakened, and AA-EVs treatment could dose-dependently restore PPARγ protein expression (Fig. 6E, F).

To further verify the above findings at the cellular level, we subsequently examined the regulatory effects of AA-EVs on lipid metabolism and PPARγ signaling in a TNF-α-induced C2C12 myotube atrophy model. Both Oil Red O staining and Nile Red staining showed that TNF-α treatment led to significant accumulation of intracellular lipid droplets, while AA-EVs co-treatment could dose-dependently alleviate lipid accumulation (Fig. 6G–J). Consistent with this, AA-EVs treatment dose-dependently reduced the intracellular MDA content and free fatty acid level elevation caused by TNF-α stimulation (Fig. 6K, L). qPCR analysis further confirmed that AA-EVs could improve the TNF-α-induced fatty acid metabolism gene disorder, restore fatty acid oxidation function, and restore PPARγ mRNA expression (Fig. 6M, N). Western blot analysis also showed that TNF-α significantly inhibited PPARγ protein expression, and AA-EVs treatment not only restored its protein level but even made it exceed that of the unstimulated control group (Fig. 6O, P).

In summary, in vivo and in vitro experiments consistently demonstrated that AA-EVs could alleviate ACLT-induced periarticular muscle atrophy by activating the PPARγ signaling pathway, enhancing fatty acid oxidation capacity, and reducing muscle lipid accumulation.

Knockdown of PPARγ Abolishes the Protective Effects of AA-EVs on Myotube Atrophy and Lipid Accumulation

To verify whether PPARγ is a key regulatory target in the muscle protective effect mediated by AA-EVs, we knocked down PPARγ in C2C12 cells by siRNA (si-PPARγ), and after confirming the knockdown efficiency at the transcriptional and protein levels (Fig. S14, S15), we further evaluated whether the ability of AA-EVs to counteract muscle atrophy was altered in the TNF-α-induced myotube atrophy model.

Giemsa staining showed that AA-EVs treatment could significantly protect against the reduction of myotube diameter induced by TNF-α, whereas after si-PPARγ transfection, the above protective effect of AA-EVs was markedly weakened, and the myotube diameter fell back to a level close to that of the TNF-α model group (Fig. 7A, B). MyHC immunofluorescence staining results were consistent with this: the MyHC fluorescence intensity after AA-EVs treatment was significantly higher than that of the TNF-α model group, but this enhancement effect almost completely disappeared after PPARγ knockdown (Fig. 7C, D). The above results indicated that PPARγ is necessary for AA-EVs to protect myotube morphology and counteract muscle atrophy.

At the level of lipid metabolism, both Oil Red O staining and Nile Red staining showed that AA-EVs could effectively reduce TNF-α-induced lipid droplet accumulation, whereas si-PPARγ transfection significantly reversed this improvement, and lipid deposition increased again to a level close to that of the TNF-α model group (Fig. 7E–H). Consistent with this, the reducing effect of AA-EVs on free fatty acid content and MDA level was also blocked by si-PPARγ (Fig. 7I, J). The above results suggest that the regulation of lipid metabolism by AA-EVs is dependent on PPARγ.

We further analyzed myogenic regulatory factors and atrophy-related markers. qPCR results showed that the effects of AA-EVs on upregulating MyoD/MyoG and inhibiting MuRF-1/Atrogin-1 were significantly attenuated after PPARγ knockdown (Fig. 7K). Western blot analysis also confirmed that the ability of AA-EVs to restore MyoG and inhibit MuRF-1 protein expression was greatly weakened by si-PPARγ (Fig. 7L, M).

In summary, PPARγ silencing could effectively reverse the protective effects of AA-EVs on myotube atrophy and lipid deposition, suggesting that PPARγ is a key signaling node through which AA-EVs simultaneously antagonize muscle atrophy and improve lipid metabolism.

AA-EVs attenuated ACLT-induced KOA

To evaluate the therapeutic effect of AA-EVs on ACLT-induced knee osteoarthritis in mice, three-dimensional micro-CT reconstruction was performed on the knee joints of mice in each group. The results showed that the ACLT model group exhibited obvious subchondral bone loss, while the AA-EVs

treatment group could significantly alleviate this loss, increase BV/TV, and its effect was comparable to that of the sham group and superior to that of the DGB-H group (Fig. 6A, B). Histopathological analysis further showed that the ACLT model group exhibited typical pathological changes of knee osteoarthritis. AA-EVs treatment could significantly alleviate the above pathological changes and significantly reduce the OARSI score, while the DGB-H group only showed partial improvement (Fig. 6A, C). In addition, immunohistochemical results showed that compared with the DGB-H group, AA-EVs could more significantly upregulate COL2 expression and simultaneously inhibit MMP13 expression (Fig. 6A, D-E). These results indicated that AA-EVs may protect the structural integrity of the knee joint and delay the progression of KOA in ACLT mice by maintaining muscle function, and the therapeutic effect is superior to that of Danggui Buxue Decoction.

4. Discussion and conclusion

Knee osteoarthritis (KOA), as a common degenerative musculoskeletal disease in orthopedics, is characterized by high morbidity and high disability rate, and brings heavy socioeconomic burden, seriously endangering patients' quality of life and public health[52]. Periarticular muscle atrophy is a common and seriously underestimated complication of KOA. It can not only predict the occurrence and development of KOA, but also run through the whole disease course, and its degree of atrophy is closely related to the progression of KOA[53]. Exercising muscles and improving muscle quality can delay or prevent KOA[54, 55]. Therefore, the therapeutic strategy targeting periarticular muscle atrophy as an intervention target is gradually becoming a new direction in the field of KOA prevention and treatment and has attracted increasing attention[56]. This study found that Astragalus-Angelica sinensis vesicles (AA-EVs) modified based on the compatibility of Danggui Buxue Decoction (DBD) can effectively antagonize TNF-α-induced C2C12 myotube atrophy, improve periarticular muscle atrophy in ACLT mice, and delay KOA progression, suggesting that it is expected to become a candidate drug for treating KOA and its accompanying muscle atrophy by targeting muscle atrophy.

Previous studies have reported that decreased periarticular muscle mass can serve as a predictor of KOA[6]. The clinical data we collected showed that as the K-L grade of KOA patients increased, the degree of periarticular muscle atrophy increased progressively. Subsequently, we further explored the relationship between the two in an animal model. The ACLT-induced KOA model with periarticular muscle atrophy has been widely reported and is well-established[9, 34]. We performed ACLT modeling on C57BL/6J mice for different time periods. The results showed that as the ACLT modeling time increased, the joint structure damage in mice became more severe, and the degree of periarticular muscle atrophy also increased, with a linear positive correlation between the two. The above evidence suggests that periarticular muscle atrophy runs through the entire course of KOA disease, and targeting muscle atrophy is expected to become an effective strategy for intervening in KOA progression.

Modern pharmacological studies have shown that various active ingredients in DBD have anti-inflammatory, antioxidant, fatty acid metabolism-regulating, muscle atrophy-ameliorating, and OA-preventing effects. Taking Astragalus as an example, the Astragalus polysaccharides contained in it not

only have significant anti-inflammatory activity, but also can antagonize muscle atrophy by activating the Akt/mTOR pathway[16], and exert OA protective effects via multiple pathways such as the GCN2/TXN axis[17], ASK1/p38 MAPK signaling pathway[57], and Fgfr2[58]; Astragaloside IV can improve myocyte energy metabolism and inhibit inflammatory response through the IRS1/Akt pathway[59], simultaneously activate PPARα to enhance fatty acid oxidation[60], and has preventive and therapeutic effects on OA[61]; Isoflavone in Astragalus exhibit strong antioxidant capacity by scavenging reactive oxygen species and regulating the Nrf2 signaling pathway[62]. Ferulic acid, ligustilide, and Angelica sinensis polysaccharides contained in Angelica sinensis also play important roles: ferulic acid possesses anti-inflammatory activity, can improve OA by regulating energy metabolism, and can regulate fatty acid metabolism and reduce lipid accumulation; ligustilide has significant anti-inflammatory effects; Angelica sinensis polysaccharides prevent and treat OA via pathways such as PI3K/AKT signaling[63] and PPARγ/SOD2/ROS[22]. The experimental results of this study also confirmed that DBD could dose-dependently improve muscle mass, muscle fiber cross-sectional area, grip strength, and motor function in ACLT mice, upregulate the expression of the myogenic differentiation marker MyoG, inhibit the expression of the atrophy-related E3 ubiquitin ligase MuRF-1, and reduce joint degeneration, delaying KOA progression. However, all indices in the DBD treatment group did not return to the sham group level, indicating obvious limitations in efficacy. This limitation is closely related to the inherent defects of the traditional water decoction process: low extraction efficiency of active ingredients, poor oral bioavailability, and insufficient lesion targeting, making it difficult for the drug to reach an effective therapeutic concentration in periarticular muscle tissue. Therefore, on the premise of retaining the essence of DBD compatibility, constructing a new drug delivery system to break through the above bottleneck has become a key issue that needs to be solved urgently.

In this study, nanovesicles were prepared from fresh Astragalus and Angelica sinensis separately, and mixed at the 5:1 compatibility ratio of DBD to obtain AA-EVs. AA-EVs exhibited typical nanovesicle morphology with an average diameter of approximately 180 nm, and maintained structural integrity in both simulated gastric fluid and intestinal fluid, indicating good gastrointestinal stability and suitability for oral administration. Coomassie brilliant blue staining and LC-MS analysis confirmed that AA-EVs completely retained the main bioactive components in As-EVs and An-EVs, including Astragaloside III, Astragaloside VI, ferulic acid, and Senkyunolide D. Based on previous studies of plant-derived nanovesicles, we demonstrated that AA-EVs could be efficiently internalized by C2C12 myotubes (24 h internalization rate reached 89.9%) without obvious cytotoxicity. Dose-response analysis identified 10–50 × 10^7 particles/mL as the optimal therapeutic concentration range, which could significantly rescue TNF-α-induced myotube diameter and viability damage (compared with the TNF-α group). Notably, CL-EVs mainly accumulated in the perinuclear region, and exhibited obvious targeting to muscle and bone tissues in vivo with significantly prolonged retention time, indicating that they have the dual potential as a therapeutic agent for improving muscle atrophy and as a drug delivery carrier for broader applications.

In the TNF-α-induced C2C12 myotube atrophy model using 100 μM TNF-α, AA-EVs treatment dose-dependently enhanced myosin heavy chain (MyHC) expression and increased myotube diameter, indicating significant recovery of myotube structure. To elucidate the regulatory effect of AA-EVs on

muscle protein turnover, we further quantitatively analyzed the transcriptional and protein translation levels of myogenic regulatory factors (MyoD, MyoG) and atrophy markers (Atrogin-1, MuRF-1). The results showed that MyoD/MyoG expression was inhibited in the TNF-α group, while Atrogin-1/MuRF-1 levels were significantly increased; AA-EVs intervention dose-dependently reversed the above changes, reflecting its restorative ability on atrophic myotubes. In the in vivo efficacy evaluation, AA-EVs demonstrated far superior therapeutic advantages over DBD. Oral administration of AA-EVs not only dose-dependently restored muscle mass, muscle fiber CSA, grip strength, and motor function in ACLT mice, but all indices in the high-dose group even completely returned to the sham group level, which was not achieved by DBD treatment. More importantly, while improving muscle atrophy, AA-EVs significantly reduced subchondral bone loss and articular cartilage degeneration, and the improvement in OARSI score was significantly better than that of DBD.

To explore the molecular mechanism of AA-EVs in combating muscle atrophy, we performed transcriptomic and metabolomic combined analysis on the quadriceps muscles of mice in the ACLT model group and the AA-EVs treatment group. The results showed that differential genes and differential metabolites were significantly enriched in entries such as lipid droplet metabolism, fatty acid metabolism, adipocyte differentiation, and PPAR signaling pathway, suggesting that fatty acid metabolism and PPAR signaling pathway may play key roles in the protective effect of AA-EVs.

Only a small amount of lipid droplets exist in normal skeletal muscle; when lipid metabolism is abnormal in muscle tissue and free fatty acid supply is excessive, lipids will undergo ectopic deposition in non-adipose tissues such as skeletal muscle, leading to the accumulation of toxic lipid intermediates (such as ceramide and diacylglycerol), triggering lipotoxicity, and further causing mitochondrial dysfunction, oxidative stress, and insulin resistance, ultimately leading to muscle atrophy[64–66]. Previous studies have shown that the rectus femoris muscle mass of C57BL/6J mice fed a high-fat diet decreases, the expression of atrophy-related genes Atrogin-1 and MuRF-1 is significantly increased, and Oil Red O staining shows obvious ectopic lipid deposition in skeletal muscle[67]. Our study also confirmed that lipid deposition in the quadriceps muscle of ACLT model mice and in TNF-α-treated C2C12 myotubes was significantly increased, and the intracellular free fatty acid content and lipid peroxidation product MDA level in C2C12 cells also increased simultaneously, while AA-EVs intervention could dose-dependently reverse the above changes. Examination of fatty acid metabolism markers and PPAR signaling in transcriptome sequencing samples showed that in the ACLT-induced KOA model with periarticular muscle atrophy, the expression of genes related to fatty acid synthesis and uptake as well as PPARα and PPARβ in skeletal muscle of model mice did not change significantly, while the expression of fatty acid oxidation-related genes and PPARγ decreased significantly; AA-EVs intervention could effectively restore the expression levels of the above oxidative genes. Moreover, studies have shown that mitochondrial fatty acid oxidation plays a key role in maintaining the functional integrity of muscle stem cells, and obstruction of this process can affect muscle regeneration and repair[68]. PPARγ, as a ligand-activated nuclear transcription factor, has been confirmed to play a key regulatory role in fatty acid metabolism, and its activation can correct fatty acid metabolism disorders and enhance fatty acid oxidation[49–51]. Furthermore, studies have reported that activating the PPARγ/PGC1α signaling axis

can promote fatty acid oxidation, promote myoblast proliferation and early differentiation, accelerate muscle regeneration, and improve muscle atrophy[69]. The above evidence suggests that PPARγ in skeletal muscle fat of ACLT mice is inhibited and acid oxidation capacity decreases, leading to aggravated ectopic lipid deposition, which in turn induces muscle atrophy. The key evidence of this study is that knocking down PPARγ by siRNA can weaken the protective effects of AA-EVs on myotube morphology, lipid accumulation, and myogenic/atrophy markers, which directly confirms that PPARγ is an indispensable mediator node for AA-EVs to exert anti-muscle atrophy effects.

Although this study has achieved encouraging findings, there are still several limitations that need to be pointed out. First, plant-derived EVs still lack recognized specific markers. This study mainly relied on electron microscopic morphology, particle size distribution, zeta potential, and positive signal of HSP70 protein for identification, and the purity assessment and batch-to-batch quality control standards need to be further established. Second, although LC-MS analysis identified 20 bioactive components in AA-EVs, which monomers or combinations are the key molecules that exert the PPARγ activation effect has not been confirmed by activity tracking separation experiments. Third, although the ACLT model used in this study can well simulate the pathological process of KOA joint instability and secondary sarcopenia, it is still different from the chronic sarcopenia accompanying primary KOA in humans. Future verification in natural aging or other KOA models will enhance the generalizability of the conclusions. In addition, issues such as the in vivo fate of AA-EVs after oral administration, the specific mechanism of crossing the intestinal barrier, and whether the regulation of gut microbiota is involved need further in-depth exploration. Follow-up studies involving microbiota transplantation will help clarify the contribution of the gut-muscle axis in the efficacy of AA-EVs.

In conclusion, this study demonstrates for the first time that fresh Astragalus-Angelica sinensis vesicles AA-EVs prepared based on the compatibility of Danggui Buxue Decoction can antagonize KOA-related periarticular muscle atrophy and delay KOA progression by activating PPARγ-mediated fatty acid oxidation and reducing muscle lipid accumulation. This finding provides a new nano-traditional Chinese medicine strategy for treating KOA by targeting muscle atrophy, and also highlights the translational potential of fresh herb-derived EVs as next-generation natural nano-biologics in the treatment of musculoskeletal diseases.

Declarations

Acknowledgements

We appreciate the great technical support from the Public Platform of Medical Research Center, of the Academy of Chinese Medical Science at Zhejiang Chinese Medical University. The authors declare that they have not use AI-generated work in this manuscript. The schematic diagrams in this study were created with BioRender.com.

Author contributions

D.W., Y.W., X.L., and J.L. contributed equally to this work. D.W., Y.W., X.L., and J.L. were responsible for investigation, experimental design, data curation, software, methodology, and writing the original draft. T.L., W.C., K.Z., X.W., H.H., J.W., and Z.B. participated in methodology and assisted with data collection and analysis. J.Y., J.C., and H.J. provided supervision, funding acquisition, and writing – review & editing. All authors reviewed and approved the final manuscript.

Funding

This work was supported by the Zhejiang Provincial Vanguard and Leading Goose Science and Technology Program (2025C02177) and the National Natural Science Foundation of China (82274280, 82394445, 82305005).

Data availability

All relevant data are available within the manuscript and its supplementary files.

Competing interests

The authors declare no competing interests.

References

1. Tang S, Zhang C, Oo WM, Fu K, Risberg MA, Bierma-Zeinstra SM, Neogi T, Atukorala I, Malfait AM, Ding C, Hunter DJ. Osteoarthritis. Nat Rev Dis Primers. 2025;11:10.
2. Esrafilian A, Chandra SS, Gatti AA, Nissi MJ, Mustonen AM, Saisanen L, Reijonen J, Nieminen P, Julkunen P, Toyras J, et al. An Automated and Robust Tool for Musculoskeletal and Finite Element Modeling of the Knee Joint. IEEE Trans Biomed Eng. 2025;72:56–69.
3. Krishnasamy P, Hall M, Robbins SR. The role of skeletal muscle in the pathophysiology and management of knee osteoarthritis. Rheumatology (Oxford). 2018;57:iv22–33.
4. De Ceuninck F, Fradin A, Pastoureau P. Bearing arms against osteoarthritis and sarcopenia: when cartilage and skeletal muscle find common interest in talking together. Drug Discov Today. 2014;19:305–11.
5. Zhang L, Zhang C, Zhang J, Liu A, Wang P, Xu J. A Bidirectional Mendelian Randomization Study of Sarcopenia-Related Traits and Knee Osteoarthritis. Clin Interv Aging. 2023;18:1577–86.
6. Dang Q, Hong Z, Zeng D, Cao P, Li S, Cen H, Wang X, Zhu Z, Han W, Wang J, et al. MRI-based radiomics to determine the role of thigh muscle quality in the development of knee osteoarthritis: A discovery and validation study. J Adv Res. 2026;79:819–31.
7. Liao CD, Liao YH, Liou TH, Hsieh CY, Kuo YC, Chen HC. Effects of Protein-Rich Nutritional Composition Supplementation on Sarcopenia Indices and Physical Activity during Resistance Exercise Training in Older Women with Knee Osteoarthritis. Nutrients 2021, 13.

8. Hughes L, Paton B, Rosenblatt B, Gissane C, Patterson SD. Blood flow restriction training in clinical musculoskeletal rehabilitation: a systematic review and meta-analysis. Br J Sports Med. 2017;51:1003–11.
9. Mao X, Lv K, Qi W, Cheng W, Li T, Sun Y, Jin H, Pan H, Wang D. Research progress on sarcopenia in the musculoskeletal system. Bone Res. 2025;13:78.
10. Liang Y, Xu Y, Zhu Y, Ye H, Wang Q, Xu G. Efficacy and Safety of Chinese Herbal Medicine for Knee Osteoarthritis: Systematic Review and Meta-analysis of Randomized Controlled Trials. Phytomedicine. 2022;100:154029.
11. Liu H, Ren J, Hu Y, Yang Y, Sun H, Fang H, Yan G, Han Y, Wang X. Multi-omics analysis reveals that Danggui Buxue decoction ameliorates benzene-induced blood deficiency syndrome via the restoration of hematopoietic lineage and remodeling of the immune microenvironment. Chin Med 2026, 21.
12. Li D, Si J, Guo Y, Liu B, Chen X, Qi K, Yang S, Ji E. Danggui-Buxue decoction alleviated vascular senescence in mice exposed to chronic intermittent hypoxia through activating the Nrf2/HO-1 pathway. Pharm Biol. 2023;61:1041–53.
13. Zhang ZT, Qi Y, Chen P, Chen L, Jiang Y, Fan Z, Guan H, Bai L, Liu J, Zhao D, Yan G. Dang-Gui-Bu-Xue decoction against diabetic nephropathy via modulating the carbonyl compounds metabolic profile and AGEs/RAGE pathway. Phytomedicine. 2024;135:156104.
14. Qin XJ, Gao F, Gao SY, Tian JY, Liu XC, Yang ZQ, Guo QH. Danggui Buxue decoction activates AMPK/PGC-1α pathway to improve chronic heart failure. J Ethnopharmacol. 2026;355:120680.
15. Tian Z, Wang Y, Liu X, Xin X, Liu S, Qu Y, Li Z, Su X, Ma D. Integrated transcriptomics and metabolomics studies reveal the therapeutic effects of Astragalus polysaccharides on cancer cachexia muscle atrophy. Sci Rep. 2025;15:26224.
16. Lu L, Huang YF, Chen DX, Wang M, Zou YC, Wan H, Wei LB. Astragalus polysaccharides decrease muscle wasting through Akt/mTOR, ubiquitin proteasome and autophagy signalling in 5/6 nephrectomised rats. J Ethnopharmacol. 2016;186:125–35.
17. Chen K, Qin C, Ji C, Yu Y, Wu Y, Xu L, Jiang Y, Zou G. Astragalus polysaccharide alleviates oxidative stress and senescence in chondrocytes in osteoarthritis via GCN2/ATF4/TXN axis. Int J Biol Macromol. 2025;310:143285.
18. Zhang S, Yuan Z, Wu H, Li W, Li L, Huang H. Network Pharmacology-Based Strategy Reveals the Effects of Hedysarum multijugum Maxim.-Radix Salviae Compound on Oxidative Capacity and Cardiomyocyte Apoptosis in Rats with Diabetic Cardiomyopathy. *Biomed Res Int* 2020, 2020:8260703.
19. Li M, Wu Y, Ye L. The Role of Amino Acids in Endothelial Biology and Function. Cells 2022, 11.
20. Huang C, Huangfu C, Bai Z, Zhu L, Shen P, Wang N, Li G, Deng H, Ma Z, Zhou W, Gao Y. Multifunctional carbomer based ferulic acid hydrogel promotes wound healing in radiation-induced skin injury by inactivating NLRP3 inflammasome. J Nanobiotechnol. 2024;22:576.

21. Li Y, Wu Y, Liang J, Chen P, Xu S, Wang Y, Jiang Z, Zhu X, Lin C, Yu Y, Tang H. Ligustilide Suppresses Macrophage-Mediated Intestinal Inflammation and Restores Gut Barrier via EGR1-ADAM17-TNF-α Pathway in Colitis Mice. Res (Wash D C). 2025;8:0864.
22. Ni S, Yi N, Yuan H, Li D, Chen X, Zhuang C. Angelica sinensis polysaccharide improves mitochondrial metabolism of osteoarthritis chondrocytes through PPARγ/SOD2/ROS pathways. Phytother Res. 2023;37:5394–406.
23. Bhalani DV, Nutan B, Kumar A, Singh Chandel AK. Bioavailability Enhancement Techniques for Poorly Aqueous Soluble Drugs and Therapeutics. *Biomedicines* 2022, 10.
24. Song S, Han H, Wang J, Pu Y, Shao J, Xie J, Che H, van Hest JCM, Cao S. Polymersome-based nanomotors: preparation, motion control, and biomedical applications. Chem Sci. 2025;16:7106–29.
25. Rome S. Biological properties of plant-derived extracellular vesicles. Food Funct. 2019;10:529–38.
26. Cong M, Tan S, Li S, Gao L, Huang L, Zhang HG, Qiao H. Technology insight: Plant-derived vesicles-How far from the clinical biotherapeutics and therapeutic drug carriers? Adv Drug Deliv Rev. 2022;182:114108.
27. Liu Z, Zhuang Y, Fang L, Yuan C, Wang X, Lin K. Breakthrough of extracellular vesicles in pathogenesis, diagnosis and treatment of osteoarthritis. Bioact Mater. 2023;22:423–52.
28. Hao S, Yang H, Hu J, Luo L, Yuan Y, Liu L. Bioactive compounds and biological functions of medicinal plant-derived extracellular vesicles. Pharmacol Res. 2024;200:107062.
29. Yan R, Li W, Zhao D, Zhao J, Ying S, Xiang L, Wang H, He T, Zhao C, Cui W, et al. Injectable microgels loaded with programmable WELNs based on mendelian randomization macroanalysis alleviate osteoarthritis by restoring the circadian rhythm. Bioact Mater. 2026;56:483–508.
30. Qi W, Yang L, Pan Y, Lv K, Zhao L, Zhang Y, Kai G, Sun Y, Pan H, Wang D. Chinese leek-derived extracellular vesicles ameliorate sarcopenia by regulating mitochondrial biogenesis and autophagy via AMPK and maintaining myosin homeostasis. J Nanobiotechnol. 2025;23:721.
31. Fu J, Liu Z, Feng Z, Huang J, Shi J, Wang K, Jiang X, Yang J, Ning Y, Lu F, Li L. Platycodon grandiflorum exosome-like nanoparticles: the material basis of fresh platycodon grandiflorum optimality and its mechanism in regulating acute lung injury. J Nanobiotechnol. 2025;23:270.
32. Zheng Y, Lei L, Liang S, Ai J, Deng X, Li YQ, Zhang TP, Pu SB, Ren YS. Protective Effect of Fresh/Dry Dandelion Extracts on APAP-Overdose-Induced Acute Liver Injury. Chin J Integr Med. 2022;28:683–92.
33. Meng J, Leung KS, Jiang Z, Dong X, Zhao Z. Establishment of GC-MS fingerprint of fresh Houttuynia cordata. Chem Pharm Bull (Tokyo). 2005;53:1484–9.
34. Cunha JE, Barbosa GM, Castro P, Luiz BLF, Silva ACA, Russo TL, Vasilceac FA, Cunha TM, Cunha FQ, Salvini TF. Knee osteoarthritis induces atrophy and neuromuscular junction remodeling in the quadriceps and tibialis anterior muscles of rats. Sci Rep. 2019;9:6366.
35. Hüttner SS, Henze H, Elster D, Koch P, Anderer U, von Eyss B, von Maltzahn J. A dysfunctional miR-1-TRPS1-MYOG axis drives ERMS by suppressing terminal myogenic differentiation. Mol Ther. 2023;31:2612–32.

36. Bodine SC, Latres E, Baumhueter S, Lai VK, Nunez L, Clarke BA, Poueymirou WT, Panaro FJ, Na E, Dharmarajan K, et al. Identification of ubiquitin ligases required for skeletal muscle atrophy. Science. 2001;294:1704–8.
37. Lightfoot AP, Sakellariou GK, Nye GA, McArdle F, Jackson MJ, Griffiths RD, McArdle A. SS-31 attenuates TNF-α induced cytokine release from C2C12 myotubes. Redox Biol. 2015;6:253–9.
38. Yeo D, Kang C, Zhang T, Ji LL. Avenanthramides attenuate inflammation and atrophy in muscle cells. J Sport Health Sci. 2019;8:189–95.
39. Li HH, Willis MS, Lockyer P, Miller N, McDonough H, Glass DJ, Patterson C. Atrogin-1 inhibits Akt-dependent cardiac hypertrophy in mice via ubiquitin-dependent coactivation of Forkhead proteins. J Clin Invest 2022, 132.
40. Weintraub H, Davis R, Tapscott S, Thayer M, Krause M, Benezra R, Blackwell TK, Turner D, Rupp R, Hollenberg S, et al. The myoD gene family: nodal point during specification of the muscle cell lineage. Science. 1991;251:761–6.
41. Lodhi IJ, Semenkovich CF. Peroxisomes: a nexus for lipid metabolism and cellular signaling. Cell Metab. 2014;19:380–92.
42. Solmonson A, DeBerardinis RJ. Lipoic acid metabolism and mitochondrial redox regulation. J Biol Chem. 2018;293:7522–30.
43. Zhou H, Zhang H, Ye R, Yan C, Lin J, Huang Y, Jiang X, Yuan S, Chen L, Jiang R, et al. Pantothenate protects against obesity via brown adipose tissue activation. Am J Physiol Endocrinol Metab. 2022;323:E69–79.
44. Digel M, Ehehalt R, Stremmel W, Füllekrug J. Acyl-CoA synthetases: fatty acid uptake and metabolic channeling. Mol Cell Biochem. 2009;326:23–8.
45. Tillander V, Alexson SEH, Cohen DE. Deactivating Fatty Acids: Acyl-CoA Thioesterase-Mediated Control of Lipid Metabolism. Trends Endocrinol Metab. 2017;28:473–84.
46. Parfenova EN, Vrdoljak N, Mosca DA, Aristizabal-Henao JJ, Kiebish MA, Minden MD, Spagnuolo PA. Targeting ABCD1 inhibits peroxisomal fatty acid oxidation to selectively eliminate acute myeloid leukemia cells. Blood. 2026;147:2930–43.
47. Tawbeh A, Gondcaille C, Trompier D, Savary S. Peroxisomal ABC Transporters: An Update. Int J Mol Sci 2021, 22.
48. Li C, Xiong L, Yang Y, Jiang P, Wang J, Li M, Wei S, Tian S, Wang Y, Zhang M, Tang J. Sorafenib enhanced the function of myeloid-derived suppressor cells in hepatocellular carcinoma by facilitating PPARα-mediated fatty acid oxidation. Mol Cancer. 2025;24:34.
49. Yang ZH, Miyahara H, Iwasaki Y, Takeo J, Katayama M. Dietary supplementation with long-chain monounsaturated fatty acids attenuates obesity-related metabolic dysfunction and increases expression of PPAR gamma in adipose tissue in type 2 diabetic KK-Ay mice. Nutr Metab (Lond). 2013;10:16.
50. Jiang Q, Jiang X, Xia SL, Bu Y, Wang Y, Wu H, Deng R. Sanmiao pill ameliorates rheumatoid arthritis via PPARγ-mediated lipid accumulation in macrophage: A multi-omics and experimental validation.

Phytomedicine. 2026;150:157697.
51. Sb Y, Liang H, Zhan P, Zheng H, Zhao Qx Z, Zj L, Hx. Shang Gk, Ji Xp: Stimulator of interferon genes promotes diabetic sarcopenia by targeting peroxisome proliferator activated receptors γ degradation and inhibiting fatty acid oxidation. J Cachexia Sarcopenia Muscle. 2023;14:2623–41.
52. Mitsou E, Klein J. Liposome-Based Interventions in Knee Osteoarthritis. Small. 2025;21:e2410060.
53. Kim J-R, Pham THN, Kim W-U, Kim HA. A causative role for periarticular skeletal muscle weakness in the progression of joint damage and pain in OA. Sci Rep 2023, 13.
54. Mo L, Jiang B, Mei T, Zhou D. Exercise Therapy for Knee Osteoarthritis: A Systematic Review and Network Meta-analysis. Orthop J Sports Med. 2023;11:23259671231172773.
55. Lange AK, Vanwanseele B, Fiatarone Singh MA. Strength training for treatment of osteoarthritis of the knee: a systematic review. Arthritis Rheum. 2008;59:1488–94.
56. Chen L, Zhou H, Gong Y, Tang Y, Su H, Jin Z, Chen G, Tong P. How Do Muscle Function and Quality Affect the Progression of KOA? A Narrative Review. Orthop Surg. 2024;16:802–10.
57. Xu J, Yu Y, Chen K, Wang Y, Zhu Y, Zou X, Xu X, Jiang Y. Astragalus polysaccharides ameliorate osteoarthritis via inhibiting apoptosis by regulating ROS-mediated ASK1/p38 MAPK signaling pathway targeting on TXN. Int J Biol Macromol. 2024;258:129004.
58. Wang J, Sun T, Zhang R, Wang T, Li Y. GelMA@APPA microspheres promote chondrocyte regeneration and alleviate osteoarthritis via Fgfr2 activation. Phytomedicine. 2025;137:156176.
59. Zhu R, Zheng J, Chen L, Gu B, Huang S. Astragaloside IV facilitates glucose transport in C2C12 myotubes through the IRS1/AKT pathway and suppresses the palmitate-induced activation of the IKK/IκBα pathway. Int J Mol Med. 2016;37:1697–705.
60. Dong Z, Zhao P, Xu M, Zhang C, Guo W, Chen H, Tian J, Wei H, lu R, Cao T. Astragaloside IV alleviates heart failure via activating PPARα to switch glycolysis to fatty acid β-oxidation. Sci Rep 2017, 7.
61. Yang J, Jiang H, Wu C, Lin Y, Tan G, Zhan J, Han L, Zhu Y, Shang P, Liu L, Liu H. Copper silicate nanoparticle-mediated delivery of astragaloside-IV for osteoarthritis treatment by remodeling the articular cartilage microenvironment. J Control Release. 2025;381:113583.
62. Song Z-L, Osama A, Ji M, He Q, Zhang B, Zhao H, Hu Y, Cai W, Fang J. Emerging of a new neuroprotective isoflavonoid with potent Keap1/Nrf2/ARE pathway activation and AChE inhibition. Bioorg Chem 2026, 168.
63. Li Y, Yang Y, Zhu L, Xie S, Guo L, Zhang Z, Zhe C, Li W, Liu F. Angelica sinensis polysaccharide facilitates chondrogenic differentiation of adipose-derived stem cells via MDK-PI3K/AKT signaling cascade. Biomed Pharmacother 2024, 179.
64. Morales PE, Bucarey JL, Espinosa A. Muscle Lipid Metabolism: Role of Lipid Droplets and Perilipins. J Diabetes Res. 2017;2017:1–10.
65. Consitt LA, Bell JA, Houmard JA. Intramuscular lipid metabolism, insulin action, and obesity. IUBMB Life. 2008;61:47–55.

66. Pereyra AS, Jevtovic F, Amorese AJ, Lin C-T, Neufer PD, Spangenburg EE, Ellis JM. High dietary fat causes muscle structural breakdown, mitochondrial dysfunction, and contractile deficits in the absence of carnitine palmitoyltransferase 2. Mol Genet Metab 2026, 148.
67. Abrigo J, Rivera JC, Aravena J, Cabrera D, Simon F, Ezquer F, Ezquer M, Cabello-Verrugio C, Golbidi S. High Fat Diet-Induced Skeletal Muscle Wasting Is Decreased by Mesenchymal Stem Cells Administration: Implications on Oxidative Stress, Ubiquitin Proteasome Pathway Activation, and Myonuclear Apoptosis. *Oxidative Medicine and Cellular Longevity* 2016, 2016.
68. Yue F, Gu L, Qiu J, Oprescu SN, Beckett LM, Ellis JM, Donkin SS, Kuang S. Mitochondrial fatty acid oxidation regulates adult muscle stem cell function through modulating metabolic flux and protein acetylation. EMBO J. 2025;44:2566–95.
69. Luo L, Chua YB, Liu T, Liang K, Chua MJ, Ma W, Goh JW, Wang Y, Su J, Ho YS, et al. Muscle Injuries Induce a Prostacyclin-PPARγ/PGC1a-FAO Spike That Boosts Regeneration. Adv Sci (Weinh). 2023;10:e2301519.

Figures

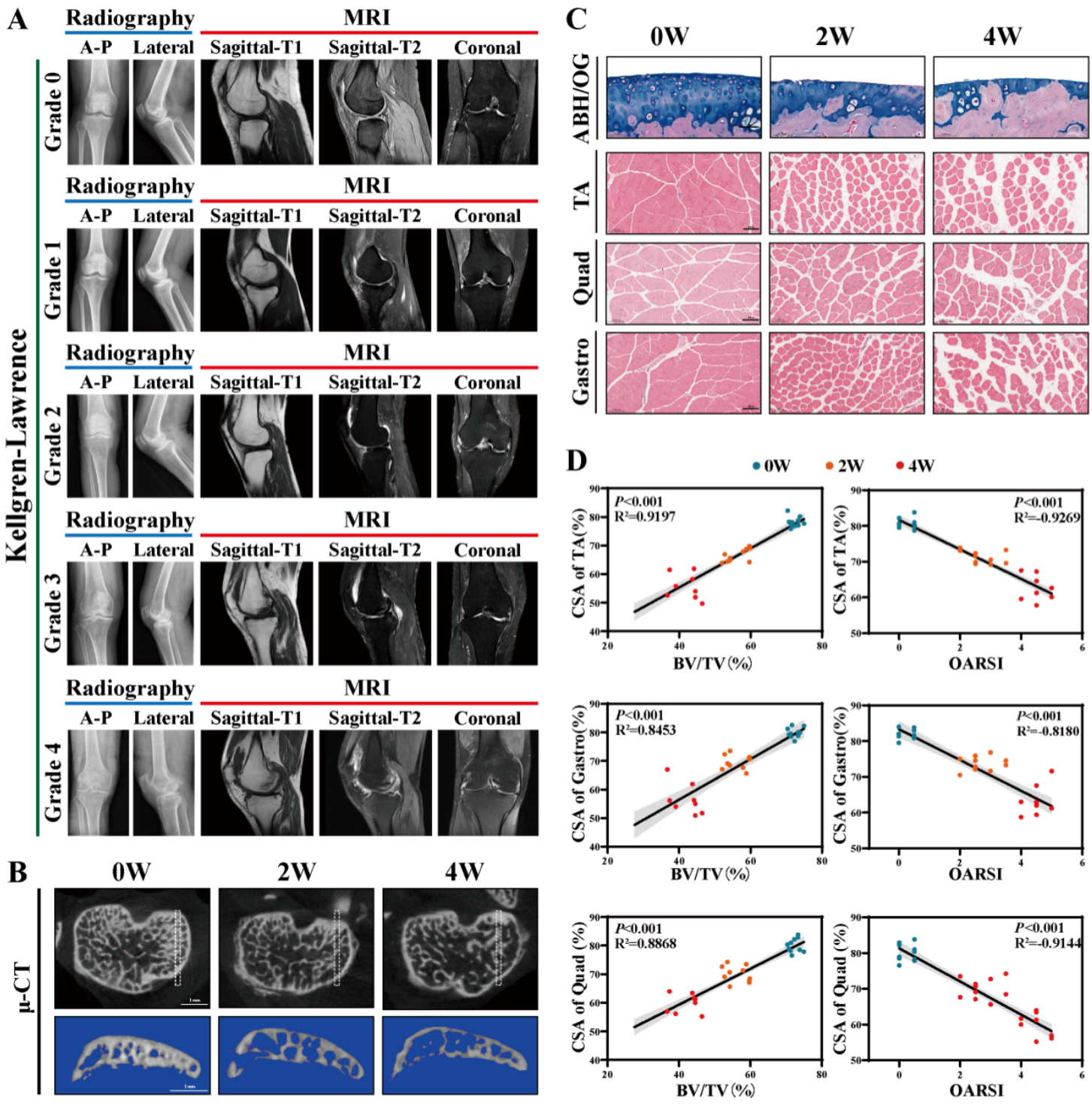


Figure 1

Periarticular muscle atrophy worsens with KOA progression. (A) Plain X-ray and magnetic resonance imaging (MRI) scans of the knee joint from patients with different KL grades. (B) Representative micro-CT images of the medial subchondral bone structure of the right knee joint. (C) ABH/OG staining of right knee joint sections, and H&E staining of cross-sections of tibialis anterior, gastrocnemius, and quadriceps muscles. (D) Linear correlation analysis between muscle fiber cross-sectional area (CSA) and BV/TV and OARSI score (n=10).

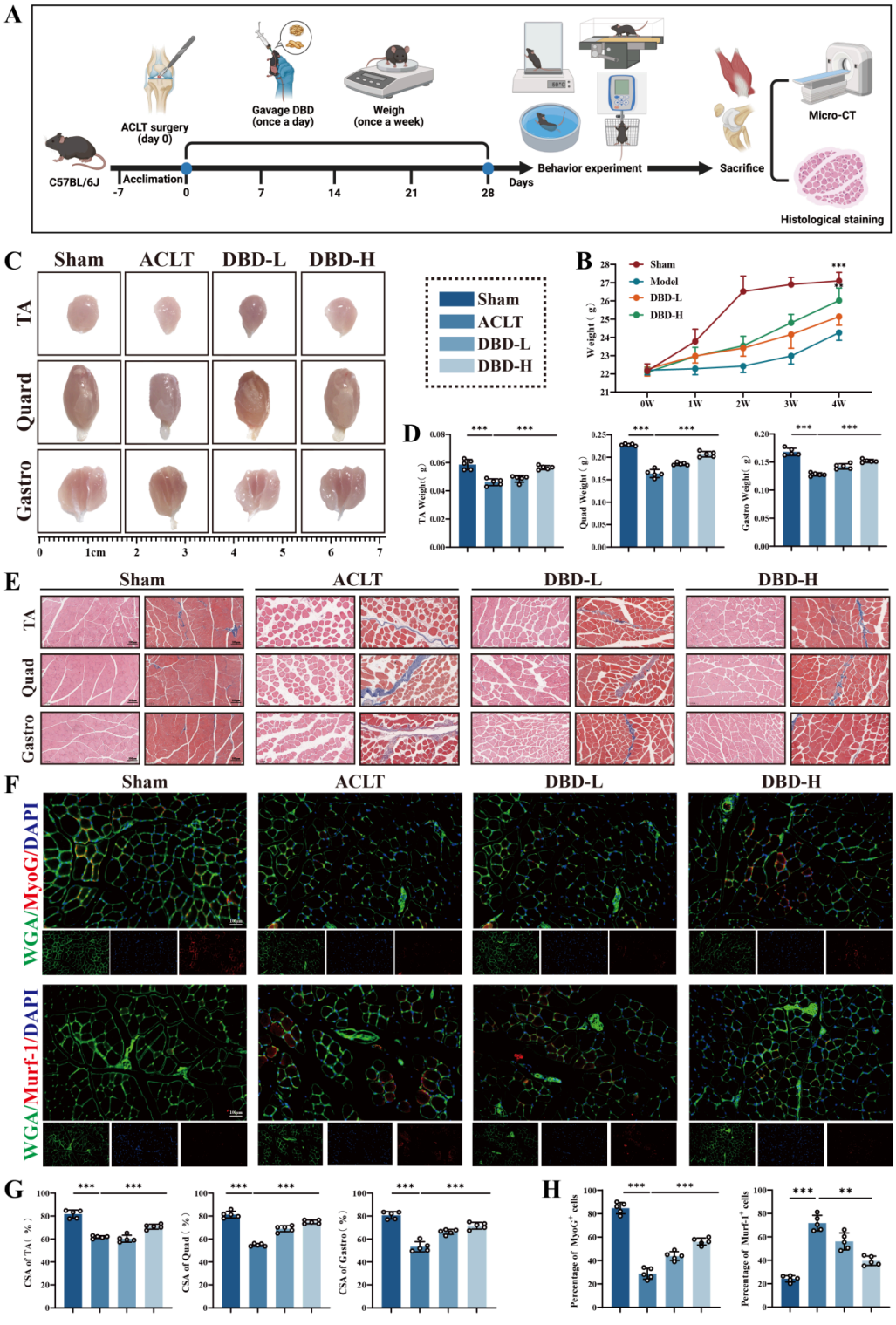


Figure 2

DBD can increase muscle mass, promote its regeneration, and improve muscle atrophy. (A) Schematic diagram of mouse ACLT model establishment and DBD treatment. (B) Statistical chart of dynamic body weight changes of mice over 4 weeks. (C) Typical photographs of the tibialis anterior, quadriceps, and gastrocnemius muscles. (D) Statistical chart of muscle mass to body weight ratio of tibialis anterior, quadriceps, and gastrocnemius muscles (n=5). (E) Cross sections of the gastrocnemius, quadriceps, and

tibialis anterior muscles were stained with H&E and Masson's trichrome. Scale bar = 100 μm. (F) Immunofluorescence staining of MyoG and Murf-1 in mouse quadriceps muscle cross sections (WGA-labeled muscle cell membrane, DAPI-labeled nucleus). (G) Statistical chart of average muscle fiber cross-sectional area of tibialis anterior, quadriceps, and tibialis posterior muscles (n=5). (H) Statistical chart of the percentage of $MyoG^+$ and $Murf\text{-}1^+$ cells in quadriceps muscle cross sections (n=5). Between-group differences were assessed using one-way ANOVA followed by Tukey's post hoc test. Asterisks denote significance levels as follows: ns, no significant; *P < 0.05; **P < 0.01; ***P < 0.001.

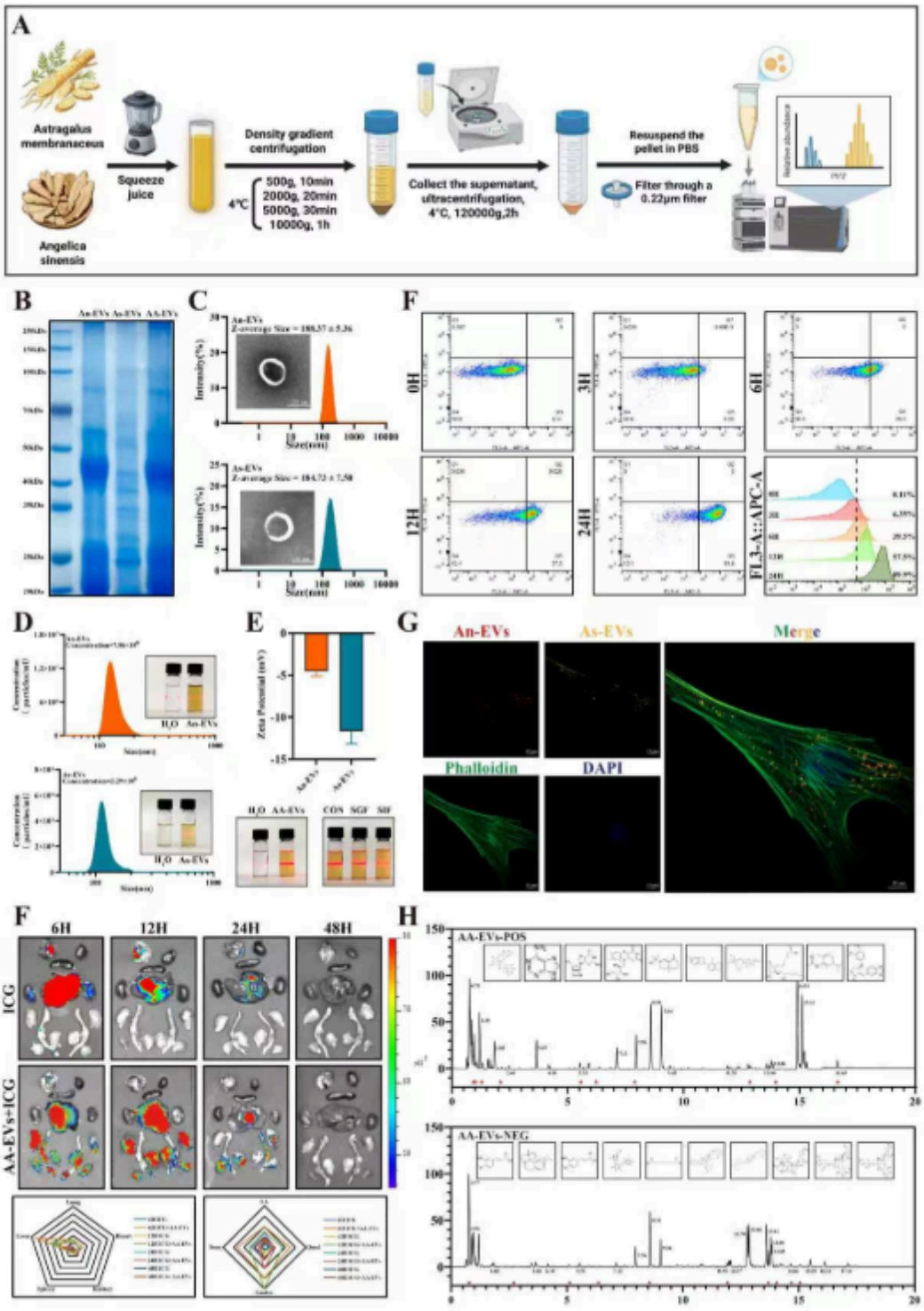


Figure 3

Isolation, Characterization, Cellular Uptake, In Vivo Retention and Targeting, and LC-MS Analysis of AA-EVs. (A)Extraction and isolation processes of AA-EVs. (B)Coomassie Brilliant Blue staining. (C)Morphological characterization of As-EVs and An-EVs by TEM, and their particle size and distribution. (D)Particle concentration and Tyndall effect of As-EVs and An-EVs. (E)Zeta potential of As-EVs and An-EVs. (F)Flow Cytometry. (G)Confocal microscopy images of C2C12 cells, As-EVs and An-EVs (DiO-labeled As-EVs in yellow, Did-labeled An-EVs in red, phalloidin-stained cytoskeleton in green, DAPI-stained nucleus in blue, and merged overlay). (H) Compounds in AA-EVs identified by LC/MS analyses in negative and positive modes.

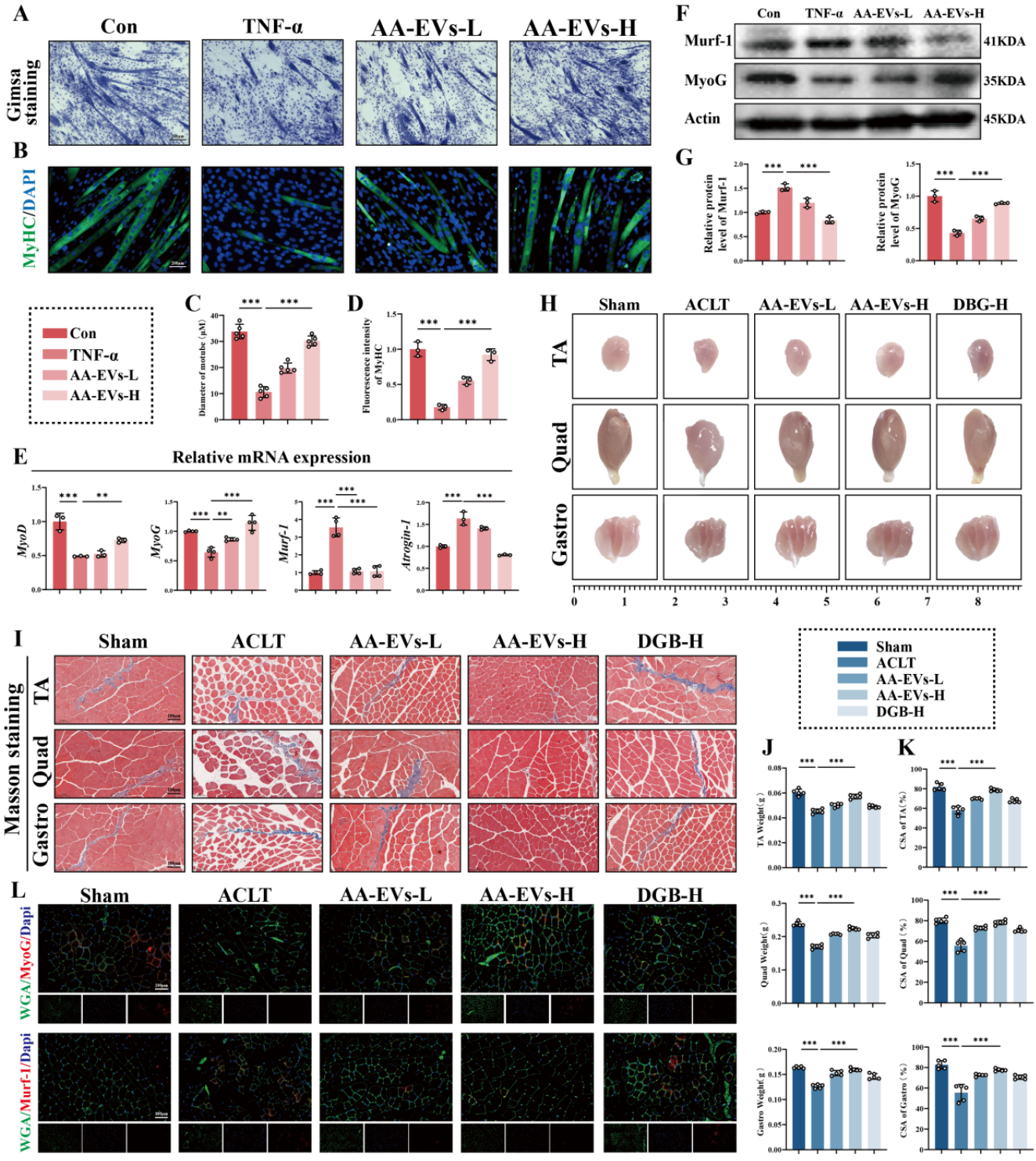


Figure 4

AA-EVs dose-dependently ameliorate ACLT-induced muscle atrophy, and their ability to promote muscle regeneration is superior to that of DBD. (A) Giemsa staining of C2C12 cells. Scale bar, 200 μm. (B) MyHC immunofluorescence staining of C2C12 cells (MyHC-labeled myotubes, DAPI-labeled nuclei). Scale bar, 200 μm. (C) Statistical chart of average myotube diameter (n=5). (D) Statistical chart of quantitative analysis of MyHC fluorescence intensity (n=3). (E) qPCR analysis of myogenic regulatory factors and

atrophy markers (n=3). (F) Western blot analysis of MyoG and Murf-1. (G) Quantitative analysis of MyoG and Murf-1 protein expression (n=3). (H) Representative images of tibialis anterior, quadriceps, and gastrocnemius muscles. (I) Masson staining of muscle cross sections (gastrocnemius, quadriceps, tibialis anterior). Scale bar, 100 μm. (J) Statistical chart of muscle mass to body weight ratio of tibialis anterior, quadriceps, and gastrocnemius muscles (n=5). (K) Statistical chart of average muscle fiber cross-sectional area of tibialis anterior, quadriceps, and tibialis posterior muscles (n=5). (L) Immunofluorescence staining of MyoG and Murf-1 in mouse quadriceps muscle cross sections (WGA-labeled muscle cell membrane, DAPI-labeled nucleus). Between-group differences were assessed using one-way ANOVA followed by Tukey's post hoc test. Asterisks denote significance levels as follows: ns, no significant; *P < 0.05; **P < 0.01; ***P < 0.001.

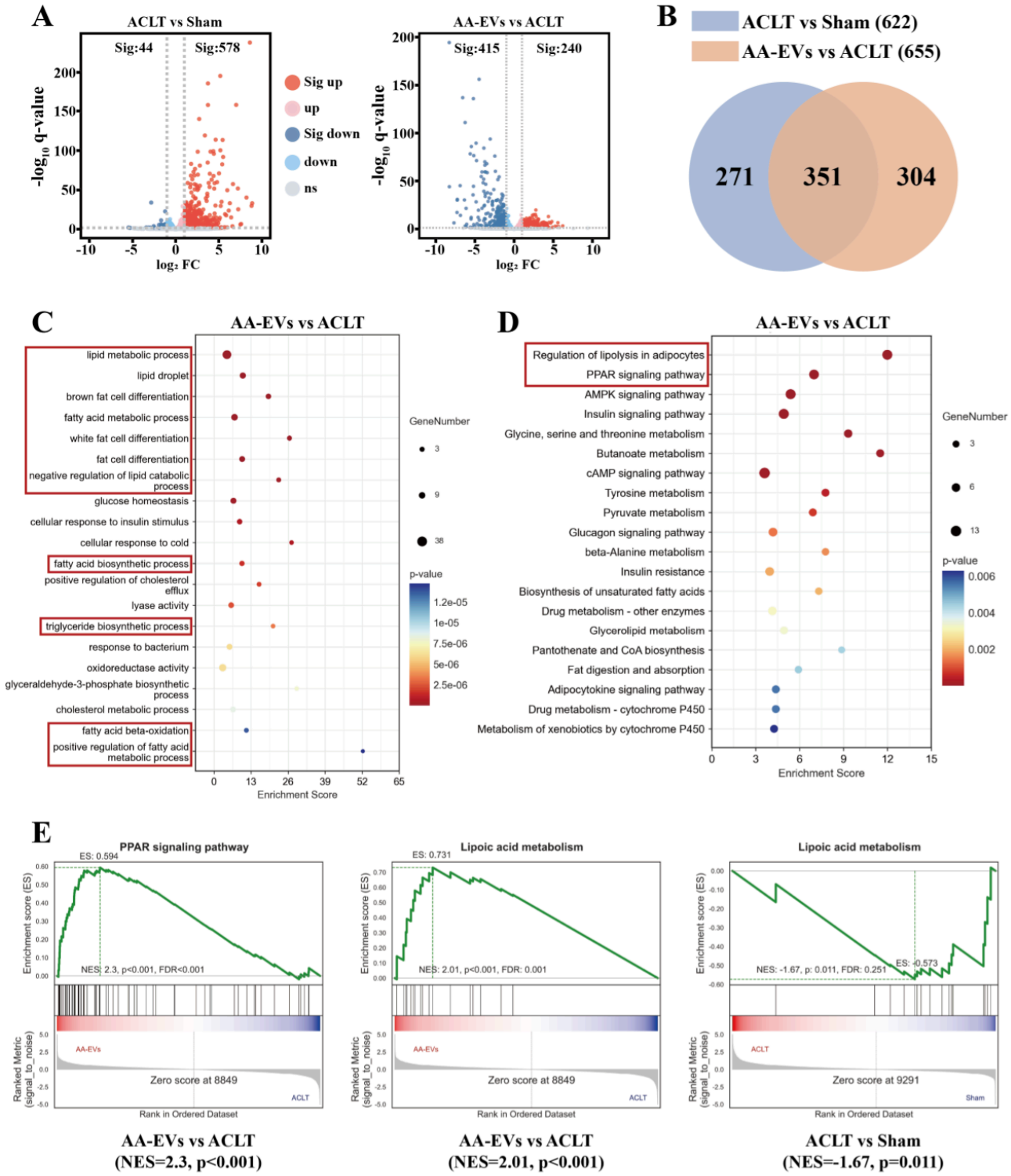


Figure 5

Transcriptomic profiling and bioinformatics analysis of quadriceps femoris muscles from ACLT-induced and AA-EVs-treated mice. (A) Volcano plots of differentially expressed genes (DEGs) in the ACLT vs. Sham and AA-EVs vs. ACLT comparisons. (B) Venn diagram showing the overlap of DEGs between the two comparisons. (C) Gene Ontology (GO) analysis of DEGs. (D) Kyoto Encyclopedia of Genes and

Genomes (KEGG) pathway analysis of DEGs. (E) Gene set enrichment analysis (GSEA) plots showing significantly enriched gene sets.

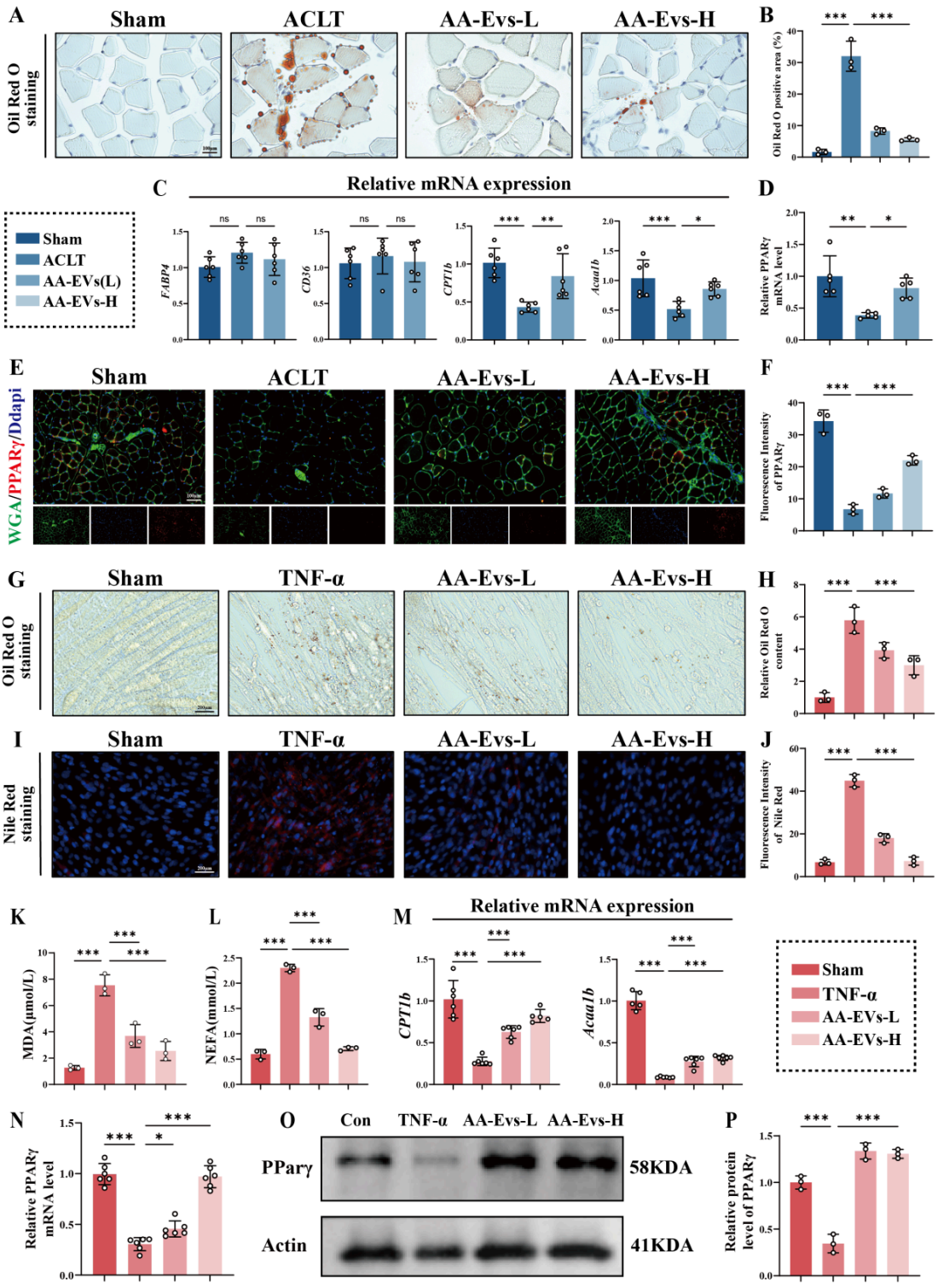


Figure 6

AA-EVs enhance fatty acid oxidation and reduce lipid deposition by activating PPARγ signaling, thereby alleviating muscle atrophy. (A) Oil Red O staining of mouse quadriceps muscle cross-sections. Scale bar,

100 μm. (B) Statistical chart of quantitative analysis of Oil Red O positive area (n=3). (C) qPCR analysis of fatty acid metabolism markers (n=6). (D) qPCR analysis of PPARγ gene (n=5). (E) Immunofluorescence staining of PPARγ in mouse quadriceps muscle cross-sections (WGA-labeled muscle cell membrane, DAPI-labeled nucleus). (F) Statistical chart of quantitative analysis of PPARγ fluorescence intensity in quadriceps muscle cross-sections (n=3). (G) Oil Red O staining of C2C12 cells. Scale bar, 200 μm. (H) Statistical chart of quantitative analysis of relative Oil Red O content in C2C12 cells (n=3). (I) Nile Red staining of C2C12 cells. Scale bar, 200 μm. (J) Statistical chart of quantitative analysis of Nile Red fluorescence intensity (n=3). (K) Detection of MDA content in C2C12 cells (n=3). (L) Detection of free fatty acid content in C2C12 cells (n=3). (M) qPCR analysis of fatty acid metabolism markers (n=6). (N) qPCR analysis of PPARγ gene (n=6). (O) Western blot analysis of PPARγ. (P) Quantitative analysis of PPARγ protein expression (n=3). Between-group differences were assessed using one-way ANOVA followed by Tukey's post hoc test. Asterisks denote significance levels as follows: ns, no significant; *P < 0.05; **P < 0.01; ***P < 0.001.

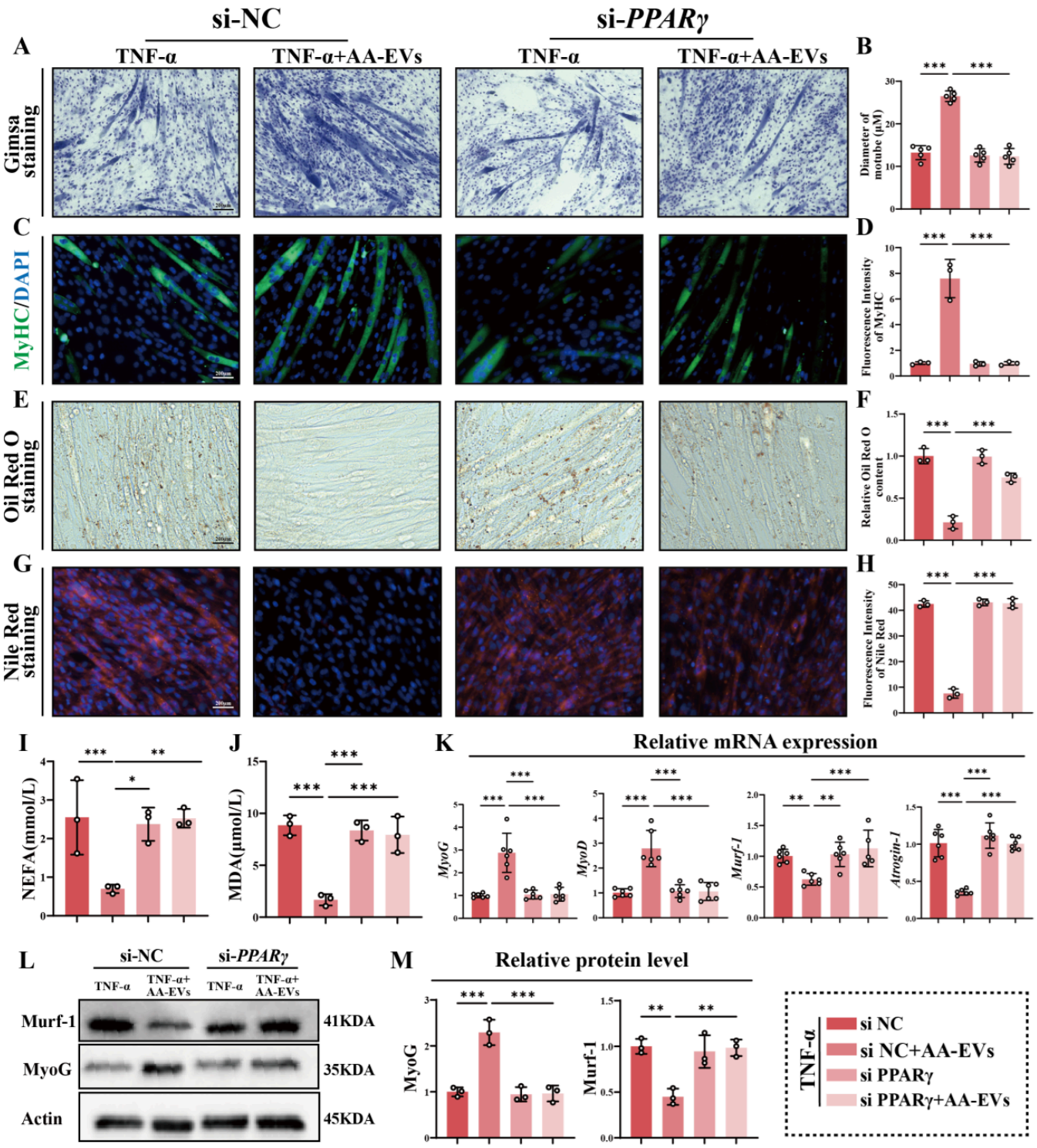


Figure 7

PPARγ knockdown abolishes the protective effects of AA-EVs on myotube atrophy and lipid accumulation. (A) Giemsa staining of C2C12 cells. Scale bar, 200 μm. (B) Statistical chart of average myotube diameter (n=5). (C) MyHC immunofluorescence staining of C2C12 cells (MyHC-labeled myotubes, DAPI-labeled nuclei). Scale bar, 200 μm. (D) Statistical chart of quantitative analysis of MyHC fluorescence intensity (n=3). (E) Oil Red O staining of C2C12 cells. Scale bar, 200 μm. (F) Statistical chart

of quantitative analysis of relative Oil Red O content in C2C12 cells (n=3). (G) Nile Red staining of C2C12 cells. Scale bar, 200 μm. (H) Statistical chart of quantitative analysis of Nile Red fluorescence intensity (n=3). (I) Detection of free fatty acid content in C2C12 cells (n=3). (J) Detection of MDA content in C2C12 cells (n=3). (K) qPCR analysis of myogenic regulatory factors and atrophy markers (n=3). (L) Western blot analysis of MyoG and Murf-1. (M) Quantitative analysis of MyoG and Murf-1 protein expression (n=3). Between-group differences were assessed using one-way ANOVA followed by Tukey's post hoc test. Asterisks denote significance levels as follows: ns, no significant; *P < 0.05; **P < 0.01; ***P < 0.001.

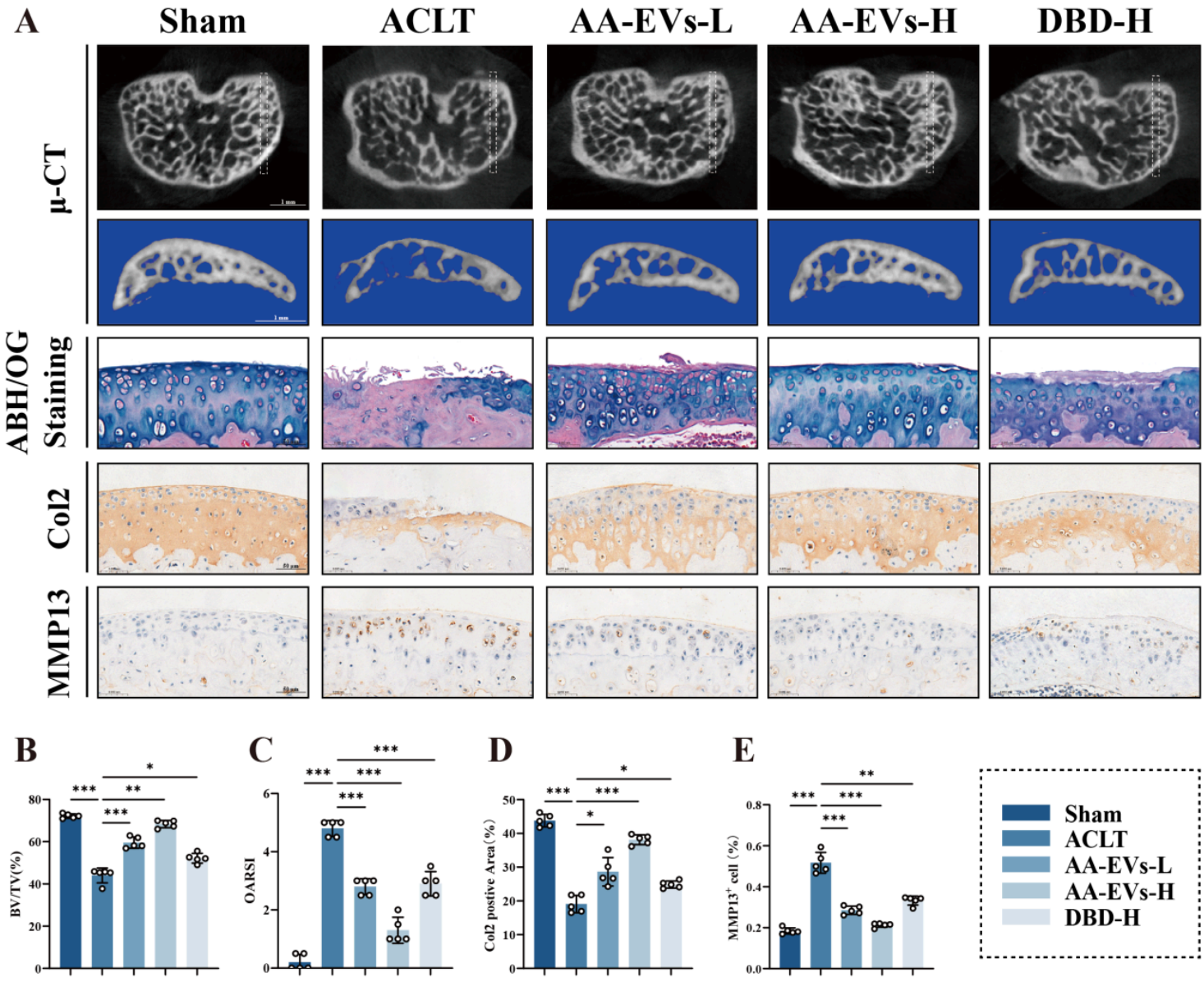


Figure 8

AA-EVs treatment significantly attenuated ACLT-induced knee osteoarthritis and exhibited superior therapeutic efficacy compared with Danggui Buxue Decoction. (A) Representative micro-CT images of medial subchondral bone architecture in the right knee, along with ABH/OG staining and

immunohistochemical detection of COL2 and MMP13 on joint sections. (B) Quantitative analysis of subchondral bone volume fraction (BV/TV). (C) OARSI histological scores of knee joints. (D) Quantification of the COL2-positive area in knee articular cartilage of each group. (E) Quantification of MMP13-positive cells in knee articular cartilage of each group. Between-group differences were assessed using one-way ANOVA followed by Tukey's post hoc test. Asterisks denote significance levels as follows: ns, no significant; *P < 0.05; **P < 0.01; ***P < 0.001.

Supplementary Files

This is a list of supplementary files associated with this preprint. Click to download.

- Supplementarymaterial.docx
- GA.png